

draft date: November 8, 2021

Properties of protostars in the Elephant Trunk globule IC 1396A

William T. Reach^{1,2}, Dohy Faied², Jeonghee Rho², Adwin Boogert¹, Achim Tappe^{2,3},
Thomas H. Jarrett^{1,2} Patrick Morris¹, Laurent Cambr esy⁴, Francesco Palla⁵, Riccardo
Valdettaro⁵

reach@ipac.caltech.edu

ABSTRACT

Extremely red objects, identified in the early *Spitzer* Space Telescope observations of the bright-rimmed globule IC 1396A and photometrically classified as Class I protostars Class II T Tauri stars based on their mid-infrared colors, were observed spectroscopically at 5.5–38 μm (*Spitzer* InfraRed Spectrograph), at the 22 GHz water maser frequency (NRAO Green Bank Telescope), and in the optical (Palomar Hale 5-m), to confirm their nature and further elucidate their properties. The sources photometrically identified as Class I, including IC1396A: α , γ , δ , ϵ , and ζ , are confirmed as objects dominated by accretion luminosity from dense envelopes, with accretion rates $1\text{--}10\times 10^{-6} M_{\odot} \text{ yr}^{-1}$ and present stellar masses $0.1\text{--}2 M_{\odot}$. The Class I sources have extremely red continua, still rising at 38 μm , with a deep silicate absorption at 9–11 μm , weaker silicate absorption around 18 μm , and weak ice features including CO_2 at 15.2 μm and H_2O at 6 μm . The ice/silicate absorption ratio in the envelope is exceptionally low for the IC 1396A protostars, compared to those in nearby star-forming regions, suggesting the envelope chemistry is altered by the radiation field or globule pressure. Only one 22 GHz water maser was detected in IC 1396A; it is coincident with a faint mid-infrared source, offset from near the luminous Class I protostar IC 1396A γ . The

¹Infrared Processing and Analysis Center, MS 100-22, California Institute of Technology, Pasadena, CA 91125

²*Spitzer* Science Center, MS 220-6, California Institute of Technology, Pasadena, CA 91125

³Harvard-Smithsonian Center for Astrophysics, 60 Garden St., Cambridge, MA 02138

⁴Observatoire de Strasbourg, Strasbourg, France

⁵NAF Osservatorio Astrofisico di Arcetri, Largo Enrico Fermi 5, 50125 Florence, Italy

maser source, IC 1396A γ_b , has luminosity $< 0.1L_\odot$, the first H₂O maser from such a low-luminosity object. Two near-infrared H₂ knots on opposite sides of IC 1396A: γ reveal a jet, with axis clearly distinct from the H₂O maser of IC 1396A: γ_b .

The objects photometrically classified as Class II, including IC1396A: β , θ , 2MASSJ 21364964+5722270, 2MASSJ 21362507+5727502, LkH α 349c, Tr 37 11-2146 and Tr 37 11-2037, are confirmed as stars with warm, luminous disks, with a silicate emission feature at 9–11 μm , and bright H α emission, so they are young, disk-bearing, classical T Tauri stars. The disk properties change significantly with source luminosity: low-mass (G–K) stars have prominent 9–11 μm emission features due to amorphous silicates while higher-mass (A–F) stars have weaker features requiring abundant crystalline silicates. A mineralogical model that fits the wide and low-amplitude silicate feature of IC1396A: θ requires small grains of crystalline olivine (11.3 μm peak) and another material to explain the its 9.1 μm peak; reasonable fits are obtained with a phyllosilicate, quartz, or relatively large ($> 10 \mu\text{m}$) amorphous olivine grains.

The distribution of Class I sources is concentrated within the molecular globule, while the Class II sources are more widely scattered. Combined with the spectral results, this suggests two phases of star formation, the first (4 Myr ago) leading to the widespread Class II sources and the central O star of IC 1396, and the second (< 1 Myr ago) occurring within the globule. The recent phase was likely triggered by the wind and radiation of the central O star of the IC 1396 H II region.

Subject headings: young stellar objects; ISM: individual (IC 1396A); ISM: globules; infrared: stars; planetary systems: protoplanetary disks

1. Introduction

Spitzer has opened widely the mid-infrared (3.6–24 μm) window for studies of star formation. In the earliest observations with the observatory, as in many subsequent ones, previously unknown, mid-infrared-bright sources have been discovered in star-forming regions. In this paper we follow up (Reach et al. 2004, Paper I) on the mid-infrared sources in the bright-rimmed globule IC 1396A, known as the Elephant Trunk Nebula, a dense globule in the large, nearby (750 pc) H II region IC 1396, which is excited by the 4 Myr-old O6 star HD 206267 (see Weikard et al. 1996). Based on comparison to measured colors to those of young stellar objects in Taurus (Kenyon & Hartmann 1995), we suggested 10 sources may

be the very early Class I stage, which is thought to only last 10^5 yr (Stahler & Palla 2004), indicating that the globule is a site of very recent star formation.

Detecting new protostars in a wide variety of star forming regions is an important expansion of previous work that by necessity has concentrated on the very closest star forming regions such as Taurus and Orion. While these nearby regions provide excellent opportunities to observe the widest range of star formation (from brown dwarfs to massive stars), they are necessarily parochial. Contrary to a long-standing common belief that the Sun formed in a quiescent region like Taurus, meteoritic evidence indicates the Sun likely formed near a high-mass star, whose H II region, winds, and supernova explosion influence the evolution and composition of the protoplanetary disk (Hester et al. 2004; Tachibana et al. 2006). To search for present-day star-forming regions similar to those in which the Sun formed, we must consider massive star forming regions. In such regions, stars can be formed by radiative driven implosion of moderately dense cores (Lefloch & Lazareff 1994), and planet-building disks are exposed to strong ultraviolet radiation (O’Dell & Wen 1994). A major goal of future star formation studies should be to determine the effects of massive stars both in triggering star formation and shaping disks around young stellar objects.

In this paper, we present follow-up observations to examine the nature of the sources in IC 1396A in more detail. New *Spitzer* mid-infrared spectra demonstrate that the photometrically extremely red objects are indeed Class I protostars, with dense, highly-optically-thick envelopes shrouding a moderately luminous core inside a dust photosphere. We show that at least one of the extremely red objects, IC 1396 A: γ , powers a molecular outflow with H₂O maser emission, characteristic of a very young ($\sim 10^4$ yr) Class 0 protostars (Furuya et al. 2001). The photometrically-classified Class II objects are compared to classical T Tauri stars, based on H α emission and mid-infrared disk spectra.

2. Observations

2.1. Spitzer Space Telescope

Mid-infrared spectra were obtained using the InfraRed Spectrograph (IRS; Houck et al. 2004) in 2004 and 2005 November. Table 1 lists the sources and IRS observing modes. The 2004 observations was adversely affected by poor pointing; the 2005 observations repeated those of the first set that had offsets between actual and expected pointing larger than half the slit width in the cross-slit direction. Spectra were taken with both the short- and long-wavelength, low-resolution mode for all sources. The brightest sources were also observed with the high-resolution mode. Observations were performed in groups (‘clusters’), and a

single bright, isolated mid-infrared source (whose coordinates were measured from the IRAC images taken in 2003 December) was used as a peak-up source for each group. Mid-infrared source brightnesses and positions were verified using the IRAC and MIPS images from Paper I. The magnitudes are reported in Table 2. With respect to the values in Paper I, significant changes include the following. Source IC 1396A: λ is significantly fainter in the IRAC 3.6 and 4.5 μm channels, because in Paper I it was confused with another nearby source that is brighter in those channels (but far fainter at 24 μm). The changed colors move the source in the color-color diagram (Fig. 3 of Paper I) from an unlabeled region into the Class 1 region. The position of source IC 1396A: κ was corrected from the typographical error (copied declination of λ).

For the basic reductions, the on-slit nods were subtracted from each other, and spectra were extracted using SMART (Higdon et al. 2004). In many cases, the nod-subtracted spectra were contaminated by other sources or bright structures in the nebula; for these, a local background subtraction was performed on each noded image. The extracted spectra from each nod position were averaged, and their uncertainties combined using the root-sum-square of each extraction’s uncertainty.

For IC 1396A: α , γ , δ , and ϵ , the low-resolution ($R = \lambda/\Delta\lambda \sim 90$) 2-dimensional Basic Calibrated Data (BCD) spectral images produced by the SSC pipeline versions S15.3.0 and S17.2.0 were used as the starting point of a customized reduction. First, the spectral and spatial dimensions were orthogonalized, and then the 2-dimensional images of the two nodding positions were subtracted in order to remove extended background emission. In some cases the background emission is highly structured or multiple sources are present in the slit, and nodding pairs could not be subtracted. Here, the background observed in nearby telescope pointings was subtracted and any residual emission was removed using the background determined from neighboring columns in the source extraction process. Some background emission lines (especially at 6.2, 17.0, and 18.7 μm) were not removed completely or were over-corrected for, which was taken into account in the interpretation of the YSO spectra. The background subtraction process also removes most of the effects of pixels with deviating dark currents (“hot pixels”). Any remaining bad pixels were replaced by values from a two-dimensional interpolation. Subsequently a fixed width (4 pixels) extraction was performed and the 1-dimensional spectra were then averaged. Then the spectra were divided by spectra of the standard star HR 2194 reduced in the same way in order to correct for wavelength-dependent slit losses. Spectral features in HR 2194 (A0 V) were divided out using the photospheric model of Decin et al. (2004). Some residual standing wave structure with a period of $\sim 1 \mu\text{m}$ observed above 20 μm was not corrected for. Finally, the Spitzer/IRS modules and ground-based spectra were multiplied along the flux scale in order to match Spitzer/IRAC 3.6 and 8.0 μm fluxes, using the appropriate filter profiles, and to provide

smooth transitions between the IRS modules.

2.2. Keck/NIRSPEC L-band Spectra

The Spitzer spectra of IC 1396A α and γ are complemented by ground-based L-band spectra obtained with the NIRSPEC spectrometer at the Keck II telescope at Mauna Kea (McLean et al. 1998) at a resolving power of $R = \lambda/\Delta\lambda=2000$. This provides an independent measure of the solid H₂O column density through the strong O-H stretching mode at 3.0 μm . The data were obtained on UT 24 July 2004 in two separate grating settings covering the 2.70-3.54 and 3.34-4.19 μm spectral ranges. The telescope was nodded on the sky in an ABBA pattern for 12 and 8 minutes for the short and long-wavelength settings respectively. The spectra were reduced in a way standard for ground-based long-slit spectra, using the nearby main sequence star HR 8208 (F0V) for telluric line correction. The final signal-to-noise values are 30 and 50 for the short and long wavelength sections, respectively. Finally, the ground-based spectra were multiplied along the flux scale in order to match the Spitzer/IRAC 3.6 μm photometry, using the appropriate filter profile.

2.3. Palomar Hale Telescope: Optical spectra

Visible spectra were obtained using the Double Spectrograph (Oke & Gunn 1982) in August 2006. Visible counterparts were identified for the Class II sources using finder charts from the Palomar Observatory Sky Survey (POSS), 2nd-generation Digitized Sky Survey; these sources were identified easily and placed in the long slit with 1'' width. For objects not visible on the POSS, offsets were performed from a nearby star, using the coordinates from the IRAC images relative to the star in the POSS. All spectra were obtained in the low-resolution mode, with a resolving power 2100 (2500) in the blue (red) portion of the spectra. A dichroic with transition at 5500 Å was used to separate light to the blue and red gratings and cameras. The blue spectrum was centered at 4400 Å, with useful range 2700-5500 Å. The red spectrum was centered at 6800 Å, with useful range 5500-7900 Å. The spectra were analyzed using IRAF and then normalized in IDL. For objects not visible on the POSS, their spectra were extracted using a reference position on the slit from a bright sources.

2.4. Green Bank Telescope

Spectroscopic observations to search for H₂O masers from fourteen mid-infrared sources in IC 1396A were performed using the National Radio Astronomy Observatory (NRAO)¹ 100-m Robert C. Byrd Green Bank Telescope. The targets were observed in multiple sessions, to allow for the possible strong variability of protostellar masers on month timescales. The observing sessions were on 2006 Aug 7 and 2006 Sep 27.

The 18-22 GHz receiver was tuned to 22.23508 GHz, and the spectroscopic observations were taken in two methods. First, each source was observed by nodding between the two beams of the receiver; this efficient technique always has the source within one of the beams, but it only works the ‘off’ beam located 3′ in azimuth is free of emission. Second, each source was observed by position-switching to a blank (in radio and mid-infrared emission) field. Both the nods and position-switched spectra were analyzed using GBTIDL. The well-known maser source S Per was observed to validate the observing technique, and it was cleanly detected with an antenna temperature 140 K, consistent with the previously-measured gain of 1.8 K/Jy and the previously-measured S Per flux of 76 Jy (Vlemmings & van Langevelde 2005).

In all cases, the nodded and position-switched spectra agreed, and for all spectra except those near IC 1396A:γ the spectra are consistent with noise. Upper limits for undetected sources were derived as follows. Each 1-min-per-beam nodded spectrum yielded an rms noise of 0.24 K antenna temperature with 0.01 km s⁻¹ autocorrelator bins after hanning smoothing. Rebinning to 0.1 (1) km s⁻¹ bins, the rms antenna temperature was 0.11 (0.04) K. Therefore, we place a 3-σ upper limit on the H₂O masers for all observed sources (except detections noted below) of 0.18 Jy peak (in 0.1 km s⁻¹ bins) and 0.07 Jy km s⁻¹ flux (in 1 km s⁻¹ bins). For sources IC 1396A:γ, α, and δ, observations were 8 times longer yielding an rms of 0.028 K, and a 3-σ upper limits of 0.05 Jy peak and 0.02 Jy km s⁻¹ flux.

Figure 1 shows the H₂O maser spectra of IC1396A:γ. This source had been previously detected by Valdetaro et al. (2005) using the Medicina telescope with 1.9′ beam. Relative to the peak flux of 33.7 Jy km s⁻¹ in 2004 Dec as observed at Medicina, the maser flux decreased by more than a factor of 10³ in 2006 Aug, the first GBT epoch. By the last GBT epoch in 2007 Jan, the maser brightness had increased, but still only to a factor of 120 less than the flux in 2004 Dec. Continued monitoring at Medicina at 7 different epochs during 2007 and in 2008 Apr yielded upper limits of 1–2 Jy, confirming that the maser has remained

¹The National Radio Astronomy Observatory is a facility of the National Science Foundation operated under cooperative agreement by Associated Universities, Inc.

faint since 2006.

The GBT observations with $33''$ beam show the maser is very close to IC1396 A: γ . A cross pattern of observations through the source shows the offset of the centroid of 22 GHz maser emission from the infrared source is $11'' \pm 11''$. High-angular-resolution VLA observations by Valdetaro et al. (2008) showed that the H₂O maser is actually $7''$ N of IC1396A: γ . The maser spot is coincident with another, fainter mid-infrared source. The VLA observations were taken in 2005 Feb, when the maser was very bright (73 Jy), and the beam size was $0.4''$ so the shift of $7''$ is highly significant.

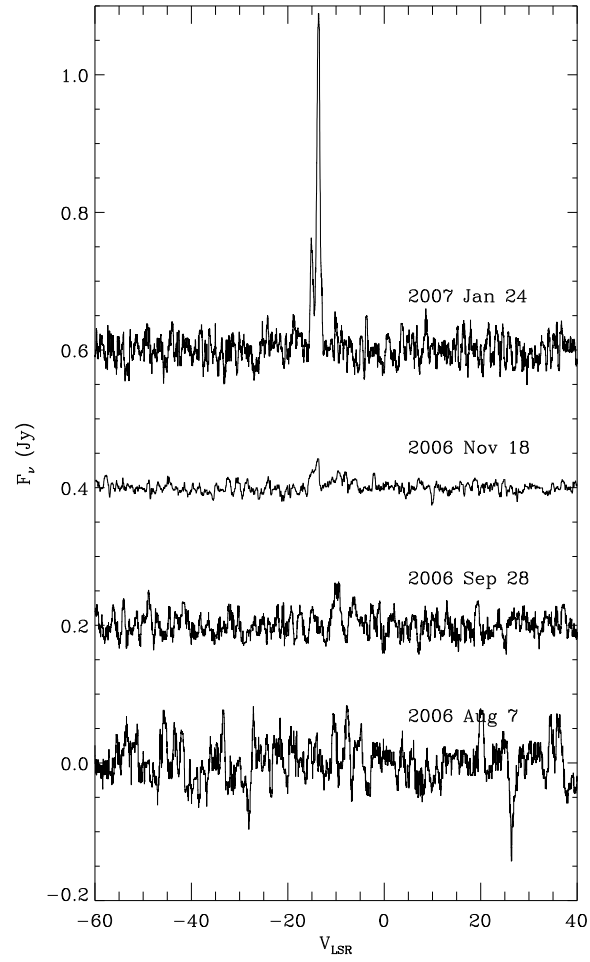


Fig. 1.— GBT 22 GHz H₂O maser spectra of IC1396A:γ on 4 dates (as labeled). The spectra are offset vertically by 0.2 Jy on each successive date, for clarity.

2.5. 2MASS

The 2 Micron All-Sky Survey (2MASS; Skrutskie et al. 2006) Extended Mission ² provides additional products to the 2MASS survey. For a few regions of the sky, including IC 1396A, 6 time exposures have been obtained. As a longer exposure time extends the completeness level by about 1 mag, there is a drawback regarding the photometric saturation which occurs for fainter sources. Consequently, photometry from the main 2MASS survey must be preferred for all saturated sources in the 2MASS 6X catalog (i.e. when the flag `rd_flg` equals 1).

We built the extinction map of IC 1396A following the method described in Cambr esy et al. (2002) using the 2MASS $H - K_s$ color excess of 32000 stars in a $40' \times 40'$ field around the nebula. Sources detected at $24 \mu\text{m}$ have been removed from the catalog since they are intrinsically red objects for which the color is not related to the cloud extinction. The extinction is obtained following the expression:

$$A_V = \left(\frac{A_H}{A_V} - \frac{A_{K_s}}{A_V} \right)^{-1} \times (H - K_s) + \mathcal{Z}_{\text{col}} \quad (1)$$

where $(A_H/A_V - A_{K_s}/A_V)^{-1} = 15.87$ (Rieke & Lebofsky 1985) and $\mathcal{Z}_{\text{col}} = -2.5$ mag. The zero point for the extinction calibration, \mathcal{Z}_{col} , corresponds to an intrinsic star color of $H - K_s = 0.16$ mag which is measured outside the nebula. Any diffuse extinction in the field is therefore removed by construction. The extinction is obtained using the median of the 10 stars included in each cell. It produces a map of IC 1396A with a resolution of about 1 arcmin, with an average visual extinction of about 5 mag. The extinction toward some specific Class II objects, which will be used later in this paper are $A_V = 5.4, 3.8, 3.5, 4.5,$ and 3.5 , for IC 1396A: $\theta, \beta, \text{Tr37 11-2037, Tr37 11-2146, and 21364964+5722270, respectively.}$

The extinction map clearly shows the central hole associated with LkH α 349 in the higher density round head of the globule. The visual extinction in the hole is 2.8 mag whereas it is ~ 6 mag in the north side of the head and ~ 10 mag for the south side with a maximum of 16.3 mag at the position 21h36m59s +57d30m00s (J2000). Beside, the correlation of the dust extinction and the emission in the Spitzer images exhibits a region with a deficit of infrared emission that corresponds to the $\sim 5'$ size structure at 21h36m +57d23m, LDN 1099. This deficit can be explained assuming LDN 1099 is disconnected from IC 1396A and located at a larger distance of the O6 heating star. This is confirmed by the examination of the optical images which suggests IC 1396A is illuminated from behind whereas L1099 would be illuminated on its front size. Assuming the system composed by

²<http://www.ipac.caltech.edu/2mass/releases/allsky/doc/explsup.html>

the O6 star, at 750 pc, and IC 1396A is seen with an angle of 45 degrees (0 degree meaning the star and the globule are at the same distance), we find the main globule IC 1396A is 4 pc closer to us than the ionizing star and that L1099 is 9 pc farther. This is confirmed by the difference of radial velocities for the two regions which are -8 km s^{-1} and 0 km s^{-1} for IC 1396A and L1099, respectively (Weikard et al. 1996).

2.6. Palomar Hale Telescope: Near-infrared images

IC 1396A was imaged using the Wide-Field Infrared Camera (WIRC; Wilson et al. 2003) on the 200" Hale telescope on 2004 Aug 25-26. The 8.7' field-of-view chip was steered toward a series of 22 positions alternating between a gradual scan across the globule and a nearby empty reference field. The reference field images were combined to generate a sky flat, which was then removed from each image. While observing, a small dither offset was added to each position to ensure that stars in the 11 reference field observations were removed during creation of the sky flat by robust averaging. The astrometry for each image was measured by comparing to the 2MASS point source catalog. Then images were combined into mosaics for each filter.

The absolute calibration of the mosaics was measured by correlating photometry in image units to the corresponding entries in the 2MASS catalog. The cross-calibration is accurate to 5%. The location of each of the sources discussed in this paper was inspected in each of the near-infrared images. Some sources that were marginally detected by 2MASS (e.g. α , γ , η , in J band) or suffered from blending with nearby sources (β) were clearly detected in the Palomar images (0.9" FWHM seeing). Table 2 (columns J and K) lists the magnitudes determined from the Palomar observations.

Figure 2 shows the near-infrared image. All of the bright Class I sources for which we obtained mid-infrared spectra are detected in this image. Two exceptionally red sources, α and γ , may be marginally resolved in the Palomar J-band image, with sizes $\sim 1.5''$ (1100 AU). In all the Palomar near-infrared images, the protostars are dominated by continuum, since their fluxes in line ($\text{Pa}\beta$ and H_2 2.12 μm) and continuum (narrow 2.17 μm and broad J) filters are similar. The resolved J-band emission is likely to be scattered light.



Fig. 2.— Near-infrared image of IC 1396A from Palomar, combining the $2.2 \mu\text{m}$ narrow continuum (red), H_2 (green), and J-band (blue). Since the H_2 and $2.2 \mu\text{m}$ continuum wavelengths are similar, point sources with spectral energy distribution rising to longer wavelengths appear red+green=yellow. The Class I protostars for which *Spitzer* spectra are presented in this paper are labeled, as are the LkH α 349 stars and the Class II star Tr 37 11-2146. The mid-infrared sources are generally ‘yellow’ in this representation, but they do not stand out based on near-infrared colors alone. The vast majority of near-infrared ‘yellow’ sources, which preferentially fall within the globule, are faint or not detected at $8 \mu\text{m}$ with IRAC (too faint for mid-infrared spectroscopy with IRS); they are probably extinguished background stars.

3. Class I Sources

3.1. Properties of the mid-infrared spectra

Figure 3 shows the spectra of the bright Class I protostars α , γ , δ , ϵ , η , and λ . Table 5 lists several properties derived from the mid-infrared spectra including colors and silicate feature amplitude. For the Class I sources, the silicate features at 10 and 18 μm are in absorption hence $\Delta F/F$ is negative; conversely for most Class II sources the silicate features are in emission.

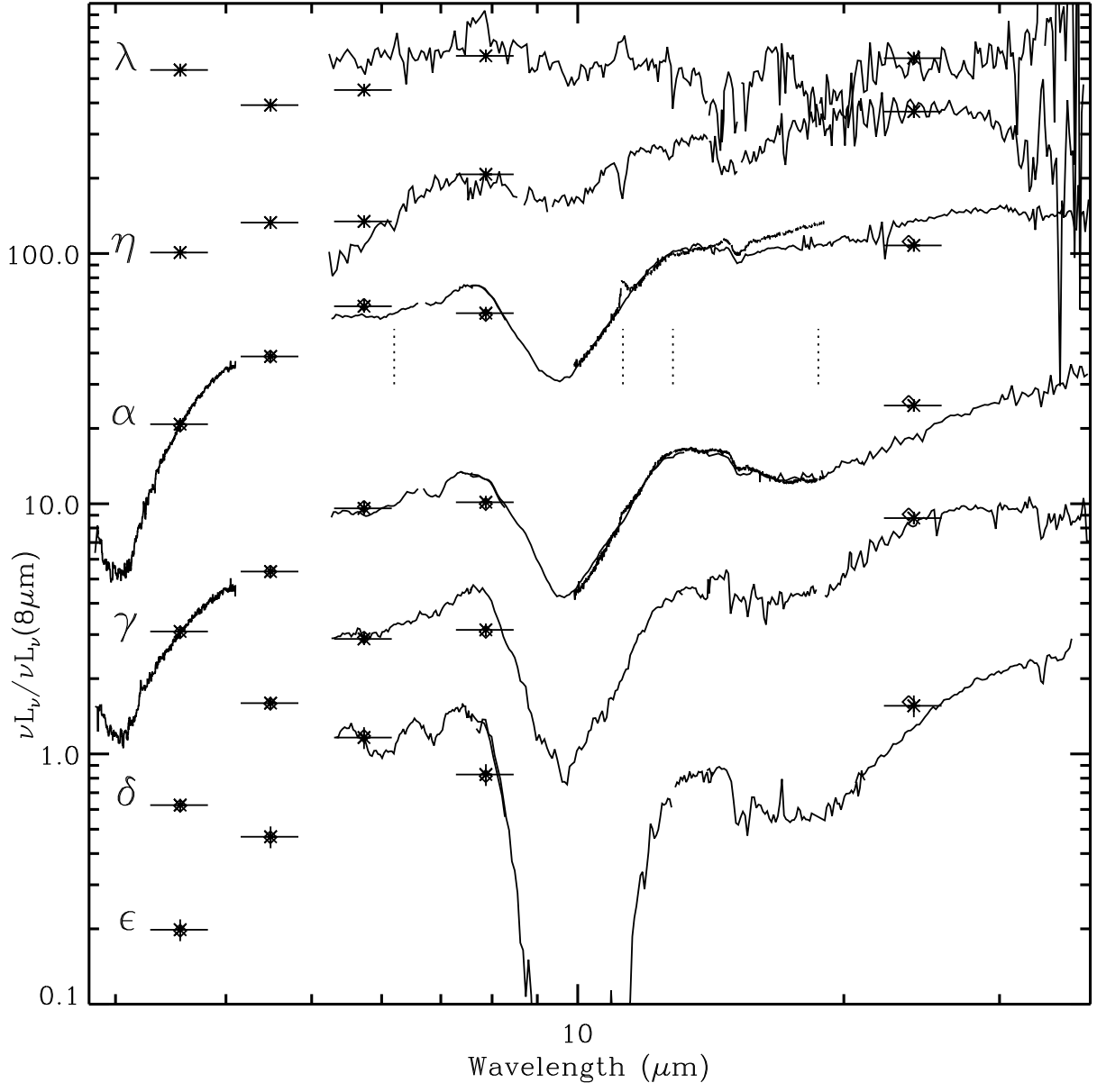


Fig. 3.— *Spitzer*/IRS spectra of Class I sources IC1396A: λ , η , α , γ , δ , and ϵ . Each spectrum is in νL_ν units, divided by its value at $8 \mu\text{m}$ and offset vertically by a factor of 3.7 for clarity. *Spitzer* and Palomar photometry are over-plotted as asterisks. For sources α and γ , IRS high-resolution spectra and Keck L-band spectra are included. For source α , the IRS high-resolution spectrum continuum does not agree with that in the low resolution-spectrum from $15\text{--}20 \mu\text{m}$; the low-resolution continuum is believed to be more accurate (and agrees with the MIPS $24 \mu\text{m}$ photometry). Narrow spikes in the spectra are due to rogue pixels and should be ignored. The positive feature in λ and α and negative dip in η at $11.2 \mu\text{m}$ are due to incomplete subtraction of a bright, nebular PAH feature; the wavelengths of nebular lines that are incompletely removed in some spectra are indicated by dotted lines at 6.2 (PAH), 11.2 (PAH), 12.8 ([Ne II]), and 18.7 ([S III]) μm .

3.2. Ice absorption features

The Spitzer spectra of IC 1396A α , γ , δ , and ϵ show the well-known ice absorption features between 5 and 8 μm , and at 15.2 μm (Fig. 3). The latter is due to solid CO_2 , while the 5–8 μm absorption is caused by the overlapping bands of many solid state species (Boogert et al. 2008). At the long-wavelength side, the 5–8 μm absorption overlaps with the edge of the strong 9.7 μm band of silicates, which complicates the determination of an overall continuum level for the study of the ice absorption features. A best-effort global continuum was determined, using all spectra and photometry available between 1 and 40 μm , similar to the method described in Boogert et al. (2008). It is kept in mind that the optical depth of the broad absorption overlying the entire 5–8 μm range shown in Fig. 4 is relatively uncertain, but that of individual, narrower, features within it is not.

The bending mode of solid H_2O peaks at 6.0 μm , but is a prominent contributor to the entire 5–8 μm absorption region. In order to determine its contribution, the H_2O column density is obtained independently from the 3.0 μm H_2O stretching mode, when available (sources α and γ) or from the 13 μm libration band (Table 6). Clearly a significant fraction of the 5–8 μm absorption is not due to the bending mode of solid H_2O (Fig. 4). The excess absorption between 5.7 and 6.6 μm is likely real, and is caused by the overlapping bands of solid H_2CO (5.7 μm), HCOOH (5.8 μm), NH_3 (6.12 μm), and possibly ions (e.g. HCOO^-) and PAH species near 6.3 μm .

At longer wavelengths, a distinct band centered at 6.9 μm is detected toward all sources. This “6.85 μm band” is commonly observed toward low- and high-mass YSOs, as well as background stars. Its profile is known to vary considerably and has been decomposed in short and long-wavelengths components (called C3 and C4 in Keane et al. 2001; Boogert et al. 2008) centered on 6.755 and 6.943 μm , respectively. The 6.85 μm bands toward the IC 1396A protostars are shifted remarkably far to longer wavelengths, i.e. C4 is much stronger than C3. Previously (Boogert et al. 2008) it was found that such sources tend to have low solid H_2O abundances, expressed in the H_2O column density scaled to the peak optical depth of the observed 9.7 μm band of silicates.

Indeed, the IC 1396A protostars have very low $N(\text{H}_2\text{O})/\tau_{9.7}$ ratios as well (Fig. 5). The origin of the components of the 6.85 μm band is not fully established, but the correlation with dust temperature tracers, such as shown in Fig. 5, suggests its carrier(s) are affected by ice processing. The NH_4^+ ion has been considered a reasonable candidate, as upon heating its band shifts to longer wavelengths and its band strength increases (Schutte & Khanna 2003). It is also more refractory than H_2O ice. Regardless of its origin, it appears that the ices toward the IC1396A protostars are thermally, and possibly energetically processed. All 4 studied YSOs show these unusual ice characteristics, which is distinct from most sources in

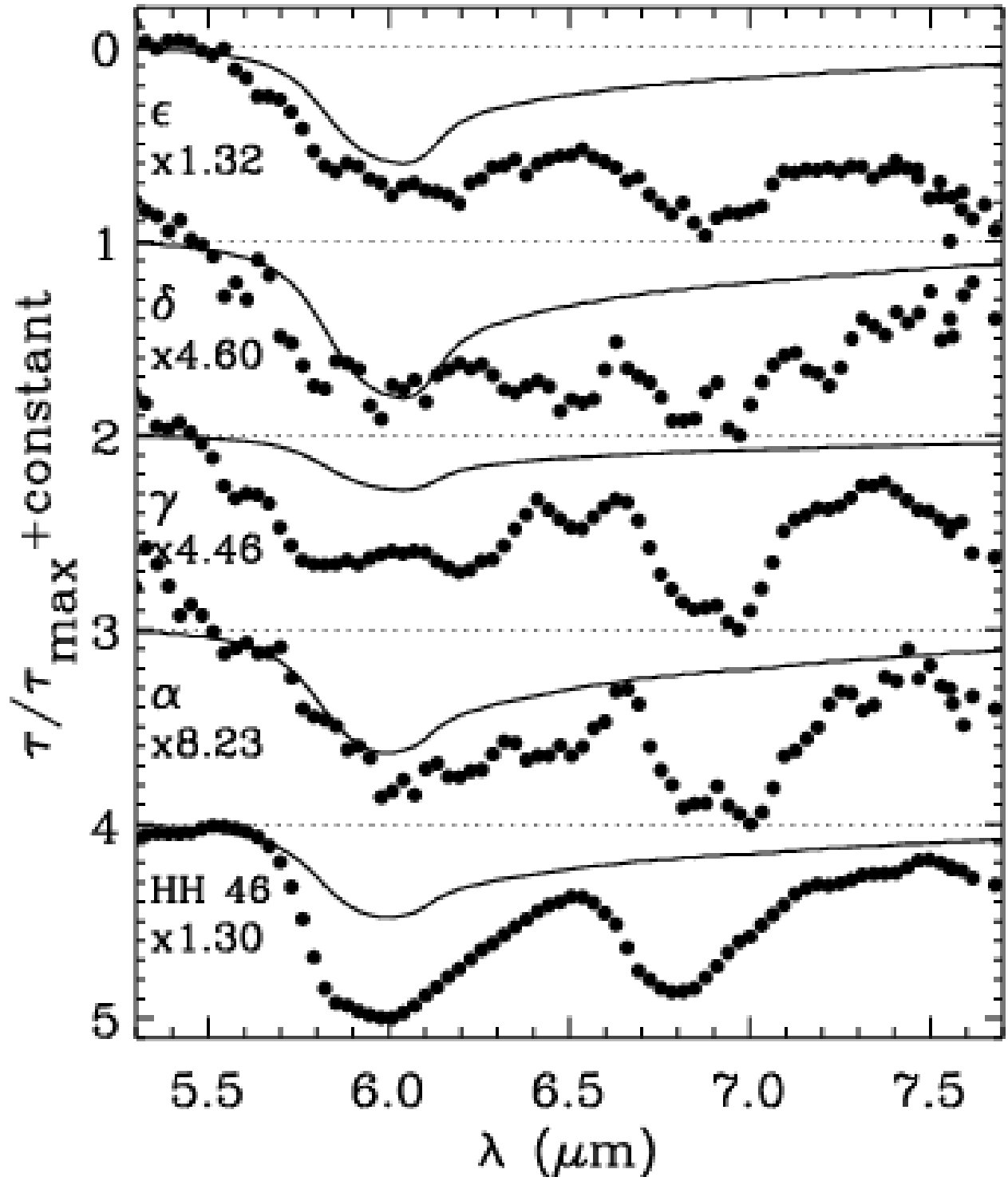


Fig. 4.— Optical depth spectra (dots) of the Class I objects in IC 1396A showing 5–8 μm absorption bands. The previously studied spectrum of the low mass YSO HH 46 IRS, representative of the large sample of low mass YSOs studied in Boogert et al. (2008), is included at the bottom. The spectra are normalized to the peak optical depth by multiplication with the factor indicated on the left, and then shifted along the vertical axis for clarity. For each source the contribution of the bending mode of pure solid H_2O is shown by a laboratory spectrum (smooth line; Hudgins et al. 1993). Note that in all IC 1396A YSOs the distinct 6.05 μm absorption band is shifted to longer wavelengths compared to HH 46 IRS.

the large sample of low mass YSOs in nearby star-forming regions studied by Boogert et al. (2008). This suggests that the ices toward IC 1396A are processed by radiation external to the YSOs, likely the harsh radiation from the nearby O star.

Finally the solid CO₂ abundances relative to H₂O are between 14-34% (Table 6), which is typical for most YSOs (Pontoppidan et al. 2008). Solid CH₃OH was looked for at 9.7 and 3.53 μm as well, but is less than 5% with respect to H₂O.

3.3. Models for the Class I protostars

We now attempt to derive the physical properties of the Class I protostars from the observed spectra and photometry. To this end, we first create a simple ‘toy’ model of a Class I object and use it to derive some fiducial parameters for the envelope. The simple model is a combination of modified blackbodies, with outer layers absorbing inner ones such as was applied to protostars in the Trifid nebula (Rho et al. 2006). Then we compare the observations to more sophisticated radiative transfer models developed by (Whitney et al. 2003), which allow us to estimate the properties of the central stars and their accretion rate. While the theoretical models are more physically detailed, they don’t fit the spectra as accurately as the simple models, which we present here as an empirical description of the data.

3.3.1. Simple model

The spectral energy distributions of the Class I sources appear to be the sum of two primary color temperatures, with the warmer component having $T_1 \simeq 420$ K and a colder component having $T_2 \simeq 120$ K. To explain the 70 μm emission, a colder component is required, with $T_3 \simeq 40$ K. As a first, empirical, description of the spectra, we will model each protostar as the sum of three nested components, with the higher temperature ones residing closer to the center and being absorbed by the colder ones:

$$F_{\nu}^{obs} = F_{\nu}^1 e^{-(\tau_2 + \tau_3)} + F_{\nu}^2 e^{-\tau_3} + F_{\nu}^3. \quad (2)$$

This simple model neglects direct emission from a potential central star, as well as neglecting details of radiative transfer. Neglecting the central star is entirely justified based on the lack of optical counterpart and the great optical depth toward the center. Neglecting radiative transfer is not justified, so one must bear in mind that the empirical models here are only descriptions of the data and not necessarily self-consistent. (More sophisticated models are described in the next section.) The optical depth of the outer layers was normalized to

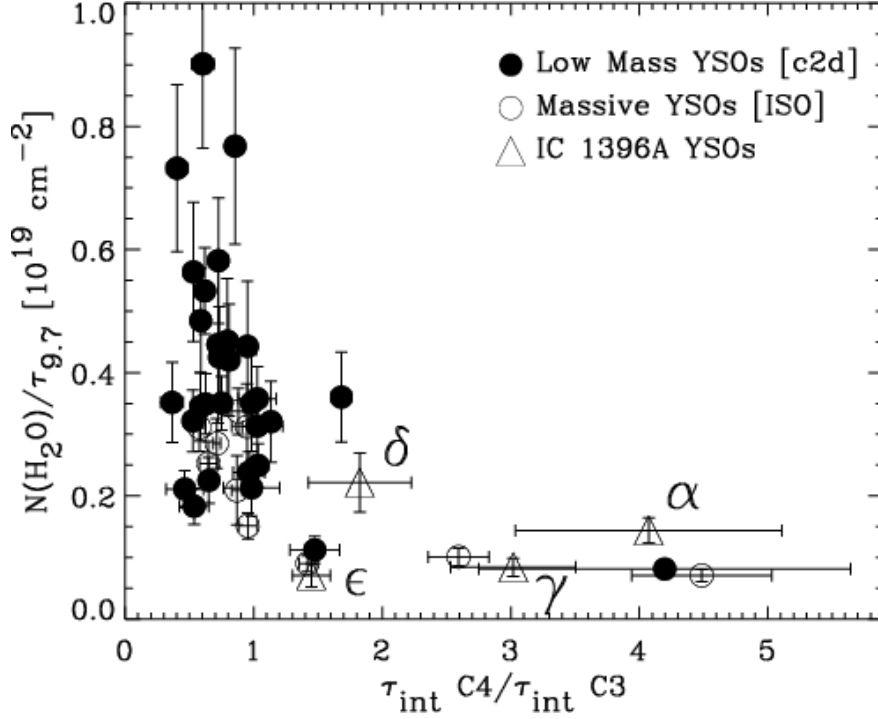


Fig. 5.— Correlation of the ratio of integrated optical depths of the components C4 and C3 of the $6.85 \mu\text{m}$ bands with a measure of the solid H_2O abundance for YSOs studied in the c2d ice survey (filled circles; Boogert et al. 2008), ISO-observed massive protostars (open circles; Keane et al. 2001) and our results for IC 1396A (triangles). All 4 YSOs in IC 1396A have strongly red-shifted $6.85 \mu\text{m}$ bands, i.e. large C4/C3 ratios and very low solid H_2O abundances. This likely implies a high degree of thermal processing of the ices in the IC 1396A core by the nearby O-star. The sources with properties overlapping with the IC 1396A protostars ($C4/C3 \lesssim 1.2$ and $\text{H}_2\text{O}/\tau_{9.7} \lesssim 0.25$) from previous studies are (from high to low C4/C3): Mon R2 IRS3, IRAS 03301+3057, S140 IRS1, DG Tau B, and W3 IRS5.

match the observed depth of the 9–11 μm silicate feature, and the wavelength-dependence of the opacity was taken from the interstellar dust model of Draine & Li (2001). The coldest component (3) was fixed at 40 K and was normalized to the difference between the observed 70 μm flux and the model for components 1 and 2 (the inner and outer envelope, respectively).

Figure 6 shows the observed spectra and empirical model fits. The color temperatures and ratio of the components 1 and 2 were adjusted to match the spectrum from 5–40 μm . We found it possible to match all the spectra with similar values of T_1 and T_2 , so we fixed them at 420 and 120 K, respectively. Specifying the 22 μm flux, F_{22} , the ratio of fluxes at 22 to 8 μm , F_{22}/F_8 , and the silicate feature optical depth, τ_{sil} was sufficient to constrain components 1 and 2. Greybody dust grains in region (2) heated by radiation from region (1) with luminosity L_1 will be at temperature

$$T_2 = 278 \left(\frac{L_1}{L_\odot} \right)^{1/4} \left(\frac{R_2}{\text{A.U.}} \right)^{-1/2} \text{ K.} \quad (3)$$

Combining the outer envelope (region 2) optical depth and size, and assuming dust/gas abundance as in the ISM, we then derive the density, n_2 , in region 2, which is of order 10^9 cm^{-3} . If the protostar is in steady accretion, then its density should follow

$$n_2 = \frac{\dot{M} R_2^{-3/2}}{4\pi\mu m_H \sqrt{2GM_*}}, \quad (4)$$

(e.g. Terebey, Shu, & Cassen 1984) from which we derive mass accretion rates of order $10^{-6} M_*^{1/2} M_\odot \text{ yr}^{-1}$. The accretion luminosity of the outer envelope alone (i.e. for initially distant material that only moves R_2) is only of order $0.1 M_* L_\odot$, less than the observed luminosity of the outer core ($L_2 \sim 1 L_\odot$). This shows that material must be accreting further in than R_2 . If the accretion luminosity arises at a radius R_{acc} , and there is a steady flow of matter inward, then

$$L_{core} = \frac{GM_* \dot{M}_{env}}{R_{acc}}, \quad (5)$$

which yields accretion radii $R_{acc} \sim 30 M_* \text{ AU}$.

The coldest component (3), or outer envelope, was fixed at 40 K and was normalized to the difference between the observed 70 μm flux and the model for components 1 and 2. including for relevant component i the visible extinction, A_V^i , the distance from the center, R_i , the volume density, n_i , and the luminosity, L_i . The opacity of the outer envelope was small, so the silicate absorption can be identified with component 2, the envelope. The volume density of the outer envelope is only an order of magnitude higher than that of a dense core (Myers, Linke, & Benson 1983), so it represents the outermost layer of the protostar that merges with the surrounding globule gas.

Table 7 lists the results of the model fits. In this empirical model, a collapsed object of radius $< 30R_{\odot}$ has formed, and it resides inside a spherical, optically thick region of size ~ 2 AU. The mass of the star cannot be readily constrained without further guidance from theoretical models. We assume masses of order $1 M_{\odot}$ for the calculations in this section. Changing to larger or smaller masses has no effect on the luminosities (which are tied to the observed fluxes), but mostly changes the size of the central object (which is hidden within the optically thick core).

The luminosity of sources α and δ arises primarily from components (1) and (2), which is consistent with these objects harboring a central protostar in the Class I phase. The luminosity of component (3), the outer envelope, is highest for γ and ϵ . The key measurement is the $70 \mu\text{m}$ flux: the ratio of $70/24 \mu\text{m}$ flux is 22, 2.6, 12, 36 for γ , α , δ , and ϵ , respectively. The $70 \mu\text{m}$ fluxes are uncertain due to the bright nebular emission and large beam; however they are sufficiently accurate to reveal differences between the sources. (Sources δ and ϵ are not cleanly resolved from each other at $70 \mu\text{m}$; the peak pixel brightnesses are comparable [with ϵ being $\sim 7\%$ brighter], so we attributed half the $70 \mu\text{m}$ flux to each source.) The origin of the $70 \mu\text{m}$ flux from γ and ϵ may be different. For γ , the presence of an H_2O maser spot $7''$ from the infrared source (see §5.2.2) indicates a Class 0 core may contribute some of the $70 \mu\text{m}$ flux we attributed to γ . For ϵ , the high $70/24 \mu\text{m}$ flux (and correspondingly, the high luminosity of component (3) in the simple model) is due to the source being more envelope-dominated, since the silicate feature is extremely deep for this source.

We can now compare this empirical, two-component description of the spectral energy distribution to a simple theoretical model for the protostar. Following Stahler & Palla (2004, hereafter SP), we expect a dust photosphere, located where the protostar is optically thick to its emergent radiation. This ‘photosphere’ will span a range of radii due to the rapid wavelength dependence of the dust opacity. To determine whether the mid-infrared emission can be associated with such a photosphere, we solve SP equations 11.12a,b using the luminosity $6 L_{\odot}$ (like source α) and an assumed mass $1 M_{\odot}$. The photospheric temperature is in the range $500 - 120$ K for a mass accretion rate in the range $0.15 - 4 \times 10^{-5} M_{\odot}$, and a photospheric radius in the range $1.4-120$ AU, respectively. These temperatures span the ‘core’ and ‘envelope’ color temperatures required to explain the $5-40 \mu\text{m}$ emission. We furthermore note that the ‘envelope’, to which we ascribed the $9-11 \mu\text{m}$ silicate absorption, has, by definition, an optical depth greater than 1 (but not greater than 10) at $10 \mu\text{m}$, so by the simplest definitions it must be considered part of the photosphere. That we required two color temperatures to match the spectral energy distribution, rather than a single blackbody, reflects only that the wavelength-dependence of the opacity leads to an extended photosphere. By ascribing the $9-11 \mu\text{m}$ silicate absorption to the cooler component, we have implicitly assumed a negative temperature gradient, as anticipated for a source powered by

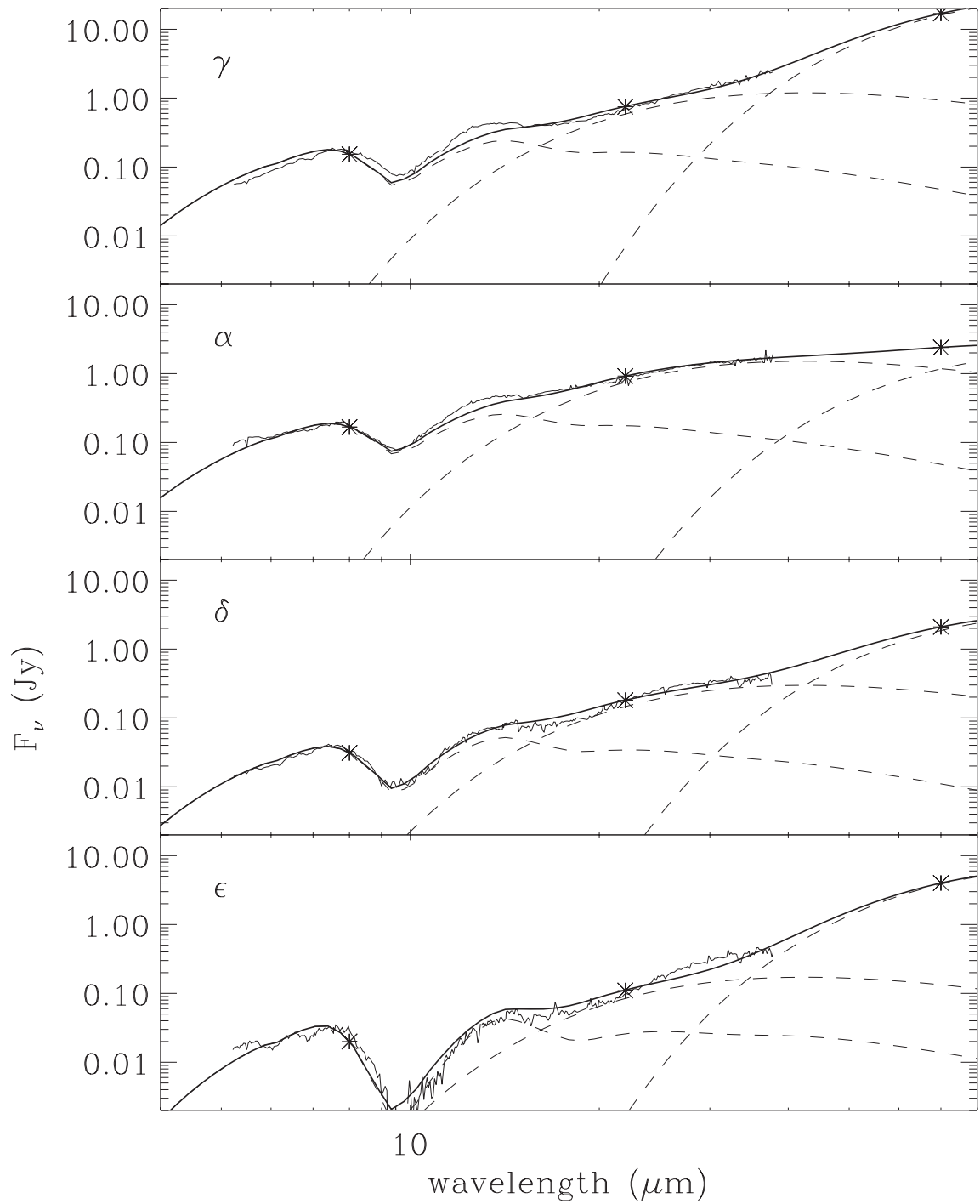


Fig. 6.— Empirical model fits to the Class I protostar spectra. For each source a sum (thick solid line) of three blackbodies (shown individually as dashed lines), with the warmest one absorbed by the cooler ones, matches the observed IRS spectra (thin solid line) and MIPS photometry (asterisk).

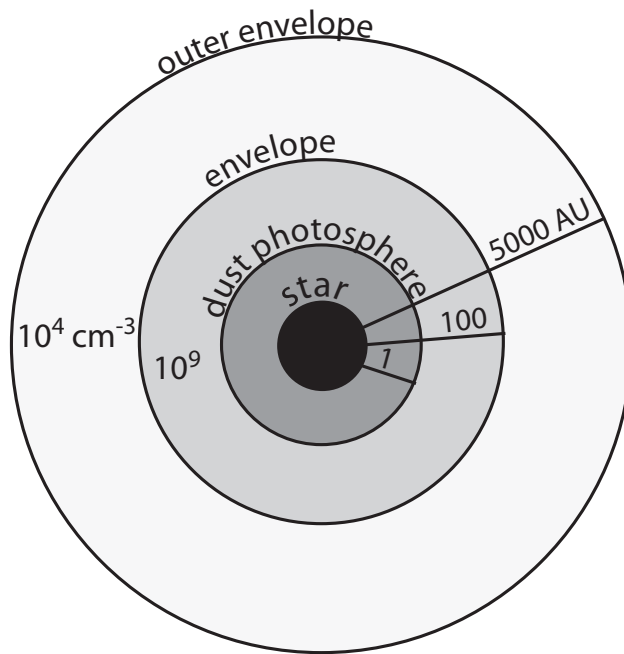


Fig. 7.— Cartoon illustrating the structure of the Class I protostars. The mid-infrared emission detected by *Spitzer* is attributed to the ‘dust photosphere’ spanning 1–100 AU and surrounded by a cooler envelope.

accretion luminosity rather than being heated by starlight and cosmic rays from the outside. Figure 7 summarizes the protostar parameters derived in this section. The agreement of the accretion rate for a simple photosphere approximation with that derived in the previous paragraph from the envelope density, and the plausibility of the protostellar radius required for accretion to provide the observed luminosity, suggest the simple protostar model presented here is at least roughly consistent with growing star surrounded by a thick envelope and powered by accretion.

3.3.2. Association with Whitney protostar models

Detailed radiative transfer models of protostars with realistic geometries have been developed by Whitney et al. (2003) and calculated over a wide range of physical parameters by Robitaille et al. (2006). To find the Whitney model that best matches the Class I source spectra, we first tabulated, for the observed spectra for sources α , γ , δ , ϵ , ζ , and η at a set of 14 wavelengths (1.22, 1.63, 2.19, 3.56, 4.51, 5.58, 7.65, 9.95, 12.93, 17.72, 24.28, 29.95, 35.06, 71.42 μm). These wavelengths were chosen to sample the SED and largely avoid ice features; however, the 12.93 μm feature possibly contains a strong H₂O libration feature which is not included in the models (Boogert et al. 2008). For each of the 2×10^5 models from Robitaille et al. (2006), we used the model fluxes integrated over the J, H, K, IRAC 3.6, IRAC 4.5, and MIPS 70m filters³, and individual model fluxes at the remaining Spitzer IRS wavelengths provided separately by T. Robitaille (personal communication). A χ^2 goodness-of-fit was calculated from the difference between the observed and model tabulated fluxes, including for each protostar model 10 possible inclination angles (87.1° [edge-on], 81.4, 75.5, 69.5, 63.3, 56.6, 49.5, 41.4, 31.8, 18.2 [pole-on]), variable ($1 < A_V < 8$ mag) line-of-sight reddening applied with the Milky Way $R_V = 3.1$ extinction curve (Weingartner & Draine 2001), and a normalization factor within the range $\pm 20\%$ relative to that appropriate for a distance of 750 pc. This procedure is very similar to the one available from Robitaille’s protostar model fitter³, and we have verified for source IC1396A α that the model identifications are in agreement. The goodness-of-fit (χ^2) was often poor, potentially due to coarseness and inapplicability of the model grid, and possible source multiplicity (IC1396A: γ discussed below). In many instances, particularly for sources IC 1396A: δ and ϵ , the large χ^2 is caused by a steeply rising MIPS 70 μm flux that was not reproduced by the models, although the rest of the SED was fitted very well. These sources are located in the southwestern rim of IC 1396A and have large fitted extinctions of $A_V \sim 7\text{--}8$ mag. We suspect that outer envelope heating by the external UV radiation field that is not accounted for in the Robitaille models

³available at <http://caravan.astro.wisc.edu/protostars/repository/index.php>

is the cause for the enhanced MIPS 70m fluxes.

The 10 models with the best χ^2 were inspected in detail for each source. Table 8 shows the most important parameters for the best-fitting model for each source. Figure 8 compares the radiative transfer model to the observed spectrum of IC1396A: α . At wavelengths longer than $10 \mu\text{m}$, the Class I protostar models are dominated by the ‘envelope,’ while at $5\text{--}8 \mu\text{m}$ the flux is mostly from the ‘disk’ in these models. The $9\text{--}11 \mu\text{m}$ silicate feature is due both to absorption of the ‘disk’ by the envelope and radiative transfer through the envelope (whose temperature decreases radially outward). Scattered light contributes significantly from $\sim 2\text{--}4 \mu\text{m}$, and emergent flux from the central star becomes dominant at wavelengths less than $2 \mu\text{m}$. It is immediately evident that these radiative transfer models are more realistic and contain more of the appropriate physics than the simple model in the previous section: no direct flux from the star would be detectable in the simple, spherical model; nor is the radiative transfer through the envelope taken into account. The detection of these sources in the near-infrared demonstrates that the envelope and/or disk must be flattened (or inhomogeneous; see Indebetouw et al. 2006), in order to allow scattered light from the star to emerge.

The properties of the central stars are not well constrained, but the model fits clearly prefer the youngest available stellar photosphere models, with ages on order 10^3 yr for α , δ and ϵ , 10^4 yr for γ and η , and 10^5 yr for ζ . The evident progression of SED shapes in Figure 3 agrees with the model fitting results, suggesting that the SED shape is sensitive to stellar age. The central star only contributes significantly to the K-band and $3.6 \mu\text{m}$ IRAC band, and it is highly extinguished. Taken at face value, the masses are similar, at $0.2\text{--}0.3 M_{\odot}$. Since the accretion rates are still high, these may not be the final masses of the young stars that will evolve toward the main sequence. If the sources remain at this accretion rate for a nominal Class I lifetime of $\sim 10^5$ yr, the added mass would be in the range $0.2\text{--}0.9 M_{\odot}$, suggesting the final masses of the stars would be in the range $0.6\text{--}1.1 M_{\odot}$.

3.3.3. Comparing the empirical and radiative transfer model results

For sources IC1396A: α and ϵ , the total luminosities obtained from the empirical (Tab. 5) and radiative transfer (Tab. 7) are in accord. The discrepancy in luminosities for γ is due to lack of an outer envelope in the radiative transfer model, or presence of a Class 0 source contaminating the $70 \mu\text{m}$ flux of γ , as discussed above. The discrepancy in luminosity for ϵ is due to lack of an outer heated envelope in the radiative transfer model. The accretion of the envelope is not included as a source of heating (see §2.2.4 of Robitaille et al. 2006).

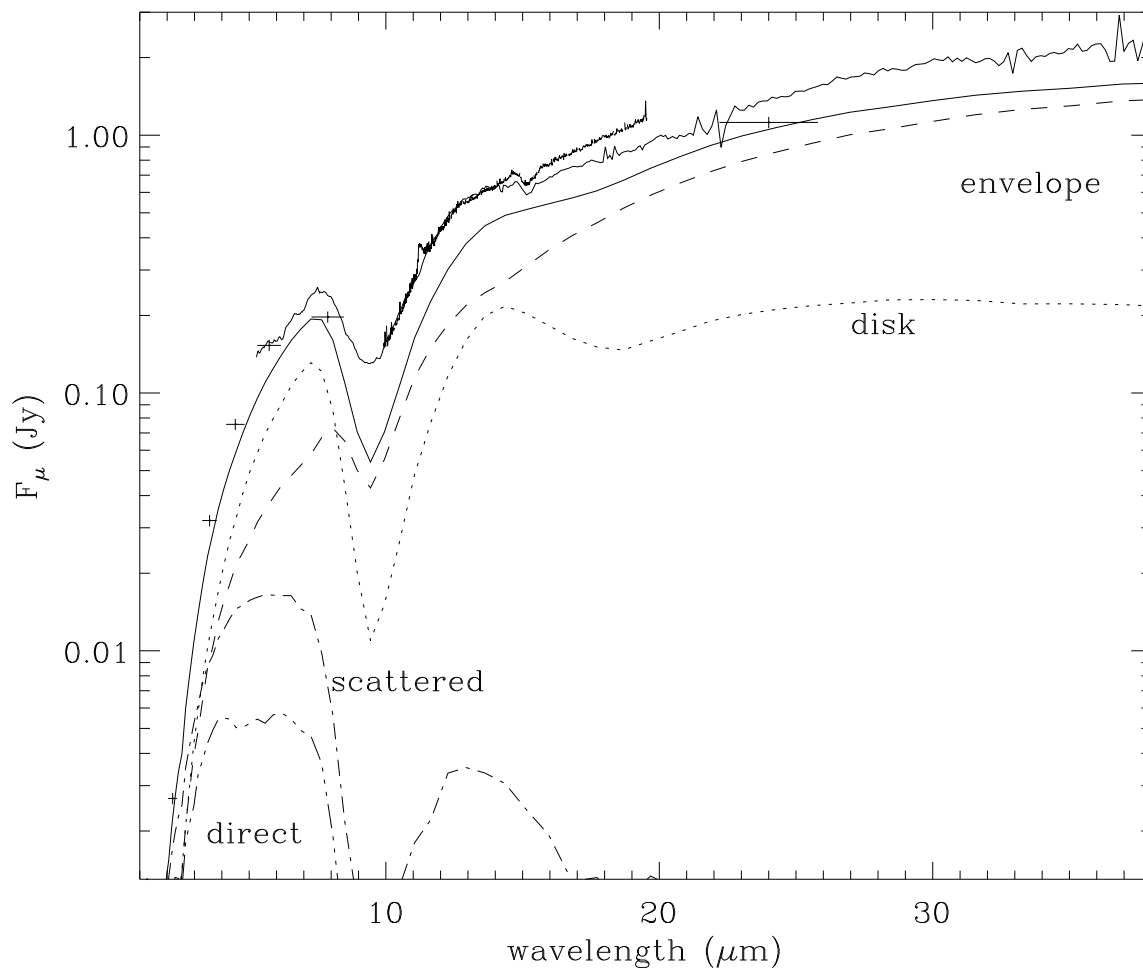


Fig. 8.— Spectrum of IC1396A α together with its best-fitting radiative transfer model from among those computed by Robitaille et al. (2006). The IRAC data are symbols with error bars; the IRS spectrum is the solid, jagged lines. Model curves are scaled downward by 10% for clarity. The model sum is a solid, smooth line. Individual model components are the outer envelope (dashed line) that contributes in the far-infrared, the inner envelope or ‘disk’ (dotted line) that contributes in the mid-infrared flux, scattered light (dash-dot line), and direct light (dash-dot-dot-dot).

The accretion rates, which are probably the most interesting quantities as they tell us how rapidly the stars are growing, are in the same order of magnitude ($10^{-6}M_{\odot} \text{ yr}^{-1}$). In both the empirical and radiative transfer models, the mid-infrared flux is dominated by the envelope, whose luminosity is determined by the accretion rate; thus the accretion rates are fairly well constrained by the observations. Nonetheless, there are some significant differences. In particular, the empirical model yields an accretion rate 9 times higher than the best-fitting radiative transfer model for ϵ . The massive outer envelope contributes 80% of the emergent luminosity in the empirical model for source ϵ . The luminosities are also in general agreement, as expected since the models were chosen to match the observations at wavelengths that span the brightest part of the spectral energy distribution. For source γ , the empirical model yields a significantly higher luminosity, due to the cold, outer component that was required to match the $70 \mu\text{m}$ flux. The Whitney models cannot match the $70 \mu\text{m}$ flux, hence the poor fit quality for γ .

4. Class II Sources

4.1. Disk Properties from the mid-infrared spectra

Figure 9 shows the spectra of four Class II sources. Each spectrum was dereddened using the line of sight extinction derived in §2.5 and a nominal $R_V = 3.1$ extinction curve (Weingartner & Draine 2001). The extinction correction is small in the mid-infrared: for $A_V = 5.4$, the optical depth $\tau = 0.14$ at the shortest IRS wavelengths ($5.5 \mu\text{m}$), 0.38 at the peak of the interstellar silicate feature ($9.5 \mu\text{m}$) and 0.06 at long wavelength ($30 \mu\text{m}$). But the line of sight extinction is high enough to block much of the optical and nearly all ultraviolet light from these young stars, making it impossible to assign spectral types using the stars’ colors.

The mid-infrared spectra in Figure 9 are characterized by a modest near-infrared brightness, a very flat continuum from $3\text{--}8 \mu\text{m}$, a bright silicate emission feature at $9\text{--}11 \mu\text{m}$, and a continuum beyond $15 \mu\text{m}$ with a range of brightnesses. Table 5 lists the colors and silicate feature strengths for the sources. The silicate feature ranges from very strong (twice the continuum) to weak (20% of continuum) to undetectable.

The radial and vertical structure of the disks can be complicated during the time of planet-building due to ejection of material from the planet growth zones as well as collection of material near stable resonances. Of particular importance for understanding formation of the Earth is the presence or lack of solid material in the $\sim 0.5\text{--}2$ AU ‘habitable’ region. For all the Class II sources with significant emission at $24 \mu\text{m}$, the color temperature of the $15\text{--}40 \mu\text{m}$ emission is around 200 K. There is no evidence of the presence of a colder disk. Given luminosities of L_* , the color temperatures suggest that the emission arises within $1.9 L_*^{1/2}$ AU of the star, corresponding to the zone of terrestrial planet formation. Emission also arises from $5\text{--}10 \mu\text{m}$, requiring dust even closer to the star.

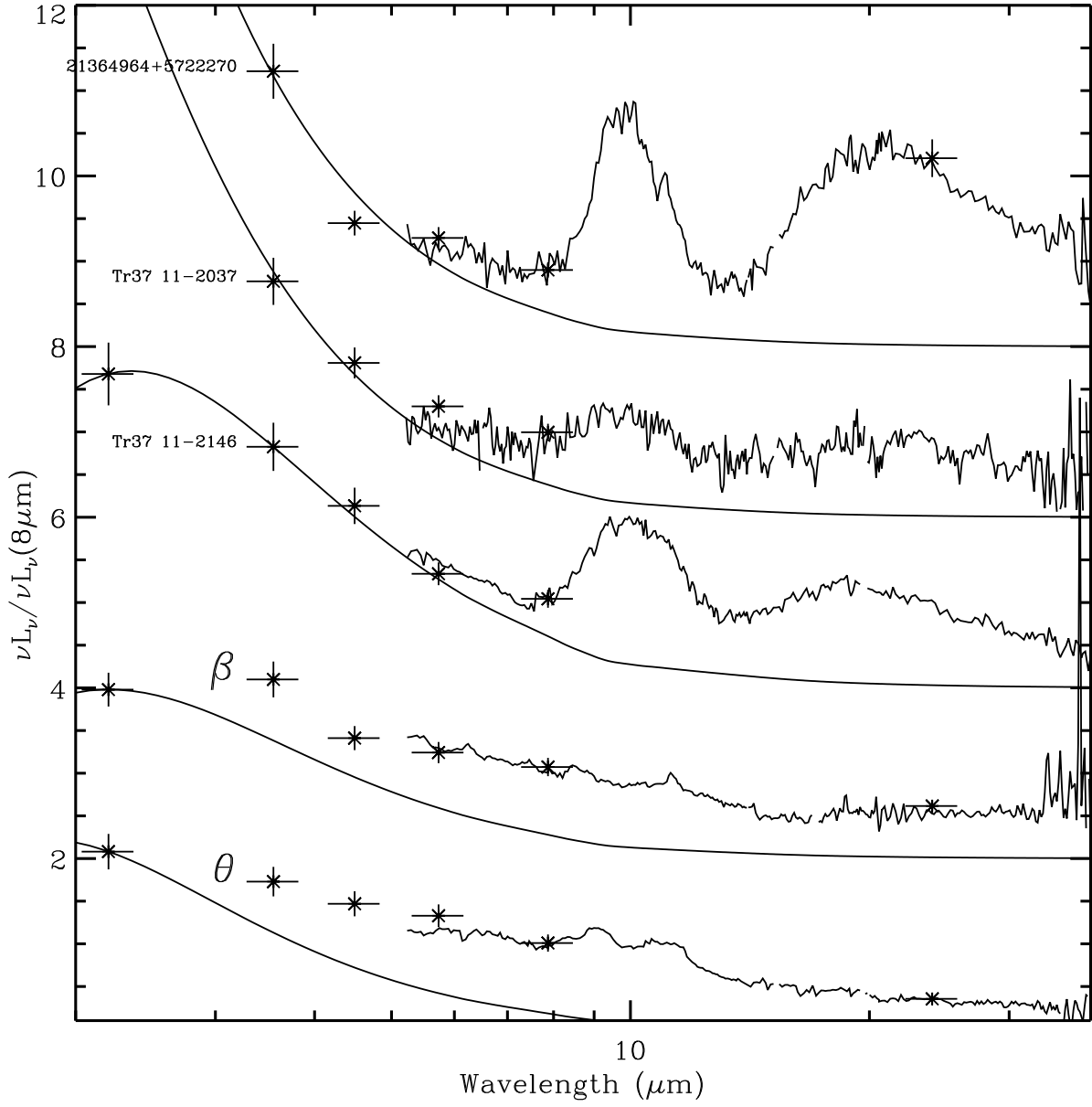


Fig. 9.— *Spitzer*/IRS spectra of Class II sources in IC 1396A. Each spectrum is in νL_ν units, divided by its value at $8 \mu\text{m}$ and offset vertically by 0, 2.5, 5, 7.5, 10 L_\odot , for sources IC1396A: θ , β , Tr37 11-2146, Tr37 11-2037, and 21364964+5722270, respectively. The solid line is a simple blackbody through the near-infrared photometry to illustrate the approximate flux of the photosphere.

Mid-infrared spectra of large samples of T Tauri and Herbig AeBe stars have been presented by Furlan et al. (2006, IRS: Taurus-Auriga), Kessler-Silacci et al. (2006, IRS: Chameleon, Lupus, and other nearby star-forming regions), Honda et al. (2006, Subaru: Taurus, TW Hydra), and Sicilia-Aguilar et al. (2007, IRS: Tr 37 and NGC 7160). Our spectra of Class II sources in IC 1396A, selected for $8 \mu\text{m}$ brightness, are generally similar to T Tauri stars in other star-forming regions. Silicate emission features are present in emission for all 5 stars in Figure 9. There are two evident morphologies of silicate features. The top 3 spectra show bright, distinct 9–11 and 18–22 μm features similar to other T Tauri stars. These features are produced by small amorphous silicate grains in an optically-thin portion of the disk, e.g. its upper surface or a flared or warped region illuminated by the star.

The bottom two stars in Figure 9, IC 1396A: θ and β , have much weaker and broader features at 9–11 μm and no evident feature at 20 μm . Both sources are bright in the IRAC and MIPS images; in the near-infrared (Fig. 2), both have nearby confusing sources. Structured nebulosity could contaminate the spectra near the PAH and important ionic lines. θ may have associated scattered light in the optical (but not in our Palomar or IRAC images). We applied local background subtractions when extracting the spectra, to minimize any contamination from the nebula or neighboring sources. The silicate features for these stars have low amplitude, but there are two peaks that are evident at the long and short-wavelength edges, making the feature appear ‘horned.’ The ‘horned’ appearance is not an effect of line-of-sight extinction. The interstellar absorption feature peaks at 9.5 μm and is broad. If the extinction to IC 1396A: θ were $A_V > 10$, then any silicate emission feature from the star would have its 9–10 μm portion depressed, generating a very “red” emission feature containing only the $\lambda > 10 \mu\text{m}$ portion. For IC1396A: θ , the two ‘horns’ are at 9.1 and 11.3 μm . The 11.3 μm horn is at the appropriate location for olivine, $\text{Mg}_x\text{Fe}_{1-x}\text{SiO}_4$. We now consider two possible explanations for the shape of the silicate feature.

First, we consider that the peaks in the feature are due to small grains of specific minerals. The 9.1 μm horn is at the approximate location for a phyllosilicate like montmorillonite $[(\text{Na},\text{Ca})_{0.33}(\text{Al},\text{Mg})_2(\text{Si}_4\text{O}_{10})(\text{OH})_2n\text{H}_2\text{O}]$ or for amorphous quartz $[\text{SiO}_2]$. We calculated absorption efficiencies for forsterite, montmorillonite, and quartz using a continuous distribution of ellipsoids (CDE) and laboratory optical constants (from Fabian et al. 2001; Glotch, Rossman, & Aharanson 2007; Henning & Mutschke 1997, respectively). A reasonable fit to the spectrum includes small grains ($< 2 \mu\text{m}$) of both crystalline forsterite and either montmorillonite or quartz, with comparable abundance, together with continuum emission at temperatures ranging from 700 to 150 K. Figure 10 compares the fit and data. The silicate feature can be explained exclusively with crystalline silicates, though the mineralogy of the larger grains cannot be distinguished. The crystalline features are emitted predominantly from the hottest part of the disk. If the luminosity is $40 L_\odot$ (as inferred from the radiative

transfer model fit discussed below), then the crystalline silicates are located about 1.6 AU from the star. The terrestrial-planet-building materials around the stars IC1396A: θ and β could therefore be rather different from most low-mass stars, even in the same globule (cf. Tr37 11-2037 and the other stars in the top of Fig. 9 that are dominated by amorphous silicates).

Second, we consider whether grain growth can explain the shape of the silicate feature. Honda et al. (2006) showed that if the grains are glassy olivine, the weaker silicate features can be explained by $\sim 2 \mu\text{m}$ grains and the stronger silicate features can be explained by $\sim 0.2 \mu\text{m}$ grains. To determine whether larger grains can explain the spectrum of IC 1396A: θ , we calculated absorption efficiencies for a range of grain sizes for glassy olivine (Dorschner et al. 1995), then optimized the disk and size to match the observed spectrum. Figure 10(a) shows the result. As noted previously, the larger grains have a flatter and wider spectra feature, eventually becoming featureless (and joining the continuum). A peak in the absorption efficiency of glassy olivine occurs around $8.6 \mu\text{m}$ for particles with radii greater than $12 \mu\text{m}$. As seen in Figure 10, the peak is at wavelengths too short to match the observed feature; however, the general shape is very similar to the observed one, and wider mineralogical search may yield a better match.

In summary, the distinctive silicate feature (weak, wide, and ‘horned’) of IC 1396A: θ and β could be due to crystalline mineralogy (with quartz or phyllosilicates providing the ‘blue’ horn of the feature) or by grain growth (with larger grains providing the width of the feature and also explaining its weakness). For wide samples of T Tauri stars, Kessler-Silacci et al. (2006, their Fig. 9), Honda et al. (2006, their Fig. 2), and Furlan et al. (2006, their Fig. 6 versus their Figs. 3–5) showed that the disks with weaker silicate features also have ‘flatter’ silicate features, where flatness is defined based on the ratio of the amplitude of the $11.3 \mu\text{m}$ olivine peak relative to the $9.8 \mu\text{m}$ amorphous silicate peak. Our results in Figure 9 also show this trend.

Furlan et al. (2006) propose an evolutionary sequence based on the mid-infrared spectral morphology, driven by dust settling and growth. In this scheme, IC 1396A: θ and β would belong to their ‘Group D’, the group with the greatest amount of grain growth. Other stars with similar spectral shapes in the star cluster include Tr 37 11-2006 and 24-515 (Sicilia-Aguilar et al. 2007). More recently, Kessler-Silacci et al. (2007) showed that the ‘flatness’ of the silicate feature is also correlated with stellar luminosity (i.e. flatter silicate features tend to be present around more luminous stars). Our data also support this trend. In particular IC1396A: θ and β are relatively luminous stars (approximate types A2 and F0) with flat features, and the later-type stars like Tr 37 11-2146 and 21364964+5722270 (K6 and G5) have stronger features.

Another possibility, as discussed above, is that the mineralogy is different, with increased abundance of phyllosilicates or quartz around the higher luminosity stars. Phyllosilicates could arise from the catastrophic disruption of a young asteroid, since aqueously altered silicates are common compositions of asteroids in particular in the outer main belt (Rivkin et al. 2002). Amorphous SiO_2 may be produced from catastrophic collisions as well, perhaps among protoplanets as suggested recently for one star (Rhee et al. 2008). It must be acknowledged that low-sensitivity infrared spectroscopy, such as presented in this paper, does not uniquely provide independent signatures of grain growth or mineralogy, because of the wide range of possible size distributions and compositions. High-quality spectroscopy of a wider sample of T Tauri stars will shed more light on this issue, which is important since the a disk bearing phyllosilicates versus a disk with moderate amounts of grain growth are such suggest distinctly different evolutionary state for the disk.

4.2. Properties of the visible spectra

The optical spectra of the Class II sample show bright $\text{H}\alpha$ emission lines, making them ‘classical’ T Tauri stars. Figure 11 shows some of the spectra. The stars appear similar to those observed by (Sicilia-Aguilar et al. 2005), suggesting they are part of the same population of T Tauri stars widespread throughout the IC 1396 region, of which IC 1396A is but a small part. Therefore, we do not elaborate upon their properties here.

4.3. Association with Whitney protostar models

The best-matching radiative transfer model from Robitaille et al. (2006) and Whitney et al. (2003) was identified using the same procedure as used for the Class I sources (§3.3.2). As was found for the Class I sources, the best-matching models for the Class II sources also had fairly high χ^2 , so the models are only to be used as a guide to plausible properties of the stars. Most of the mid-infrared-selected Class II sources are of order solar mass, with moderate-mass and slowly growing disks and negligible envelope. The two known T Tauri stars, LkH α 349a and c are fit by 2.2 and 0.7 M_\odot stars. The main difference between them is that LkH α 349c has a massive disk.

One Class II source whose model stands out from the others in terms of luminosity and mass is IC1396A: θ . Its mid-infrared spectrum is very flat, and it could not be fit by low-mass models as could the others. The best fit model was a pre-main-sequence A star ($5M_\odot$). Such a star has a large predicted photospheric decrement at 4000 Å that is not observed

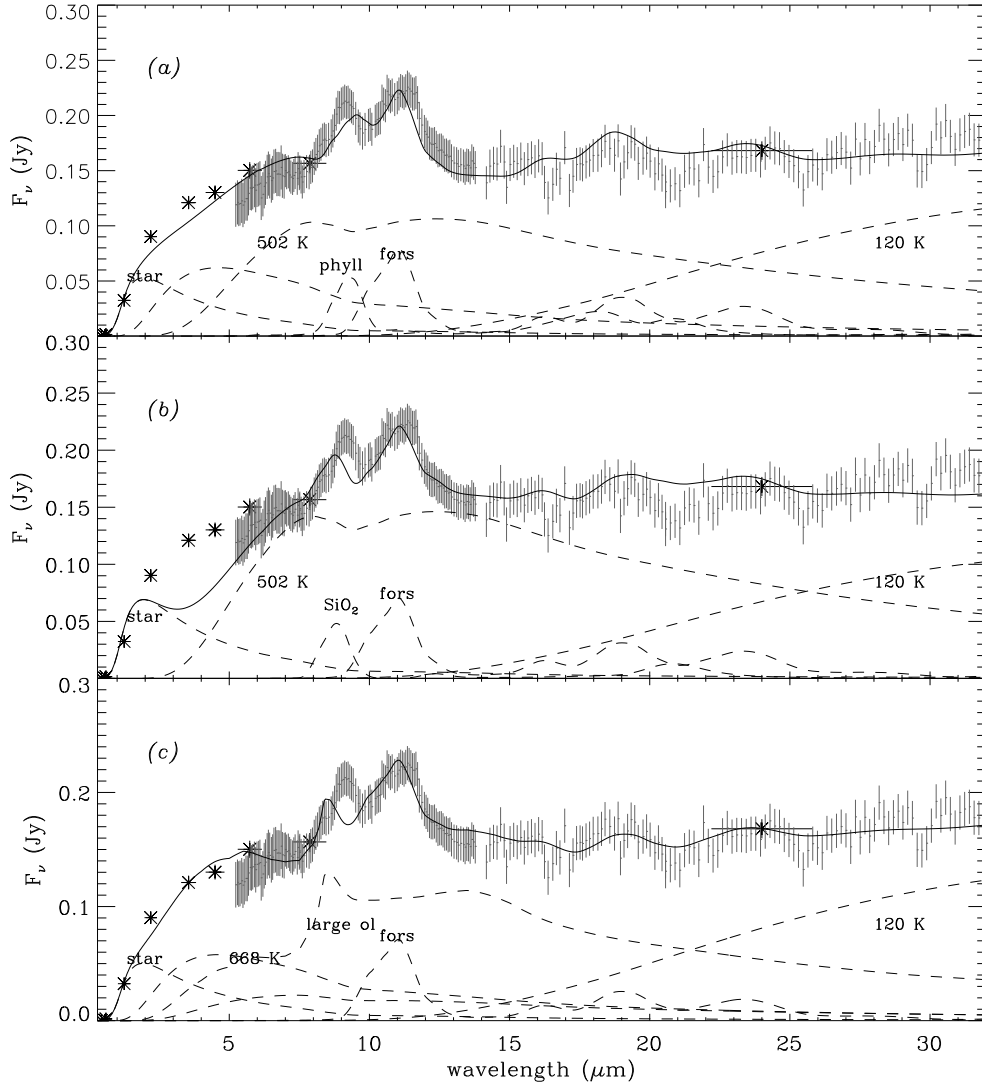


Fig. 10.— Spectrum of IC 1396A: θ together with three mineralogical fits. Panel (a) shows a combination of small (radius $< 1 \mu\text{m}$) crystalline olivine (forsterite; labeled ‘fors’) and phyllosilicate (montmorillonite; labeled ‘phyl’) particles. Panel (b) shows a combination of small crystalline olivine and large (radius $15 \mu\text{m}$) glassy olivine particles (labeled ‘large ol’). The minerals were placed at the same temperature, optimized in the range 500–800 K (as labeled) and combined with blackbody continua at 1200 and 120 K, as well as the extinguished stellar photosphere. Individual components of the spectral model are shown as dashed lines with labels, and the model sum is shown as a solid line.

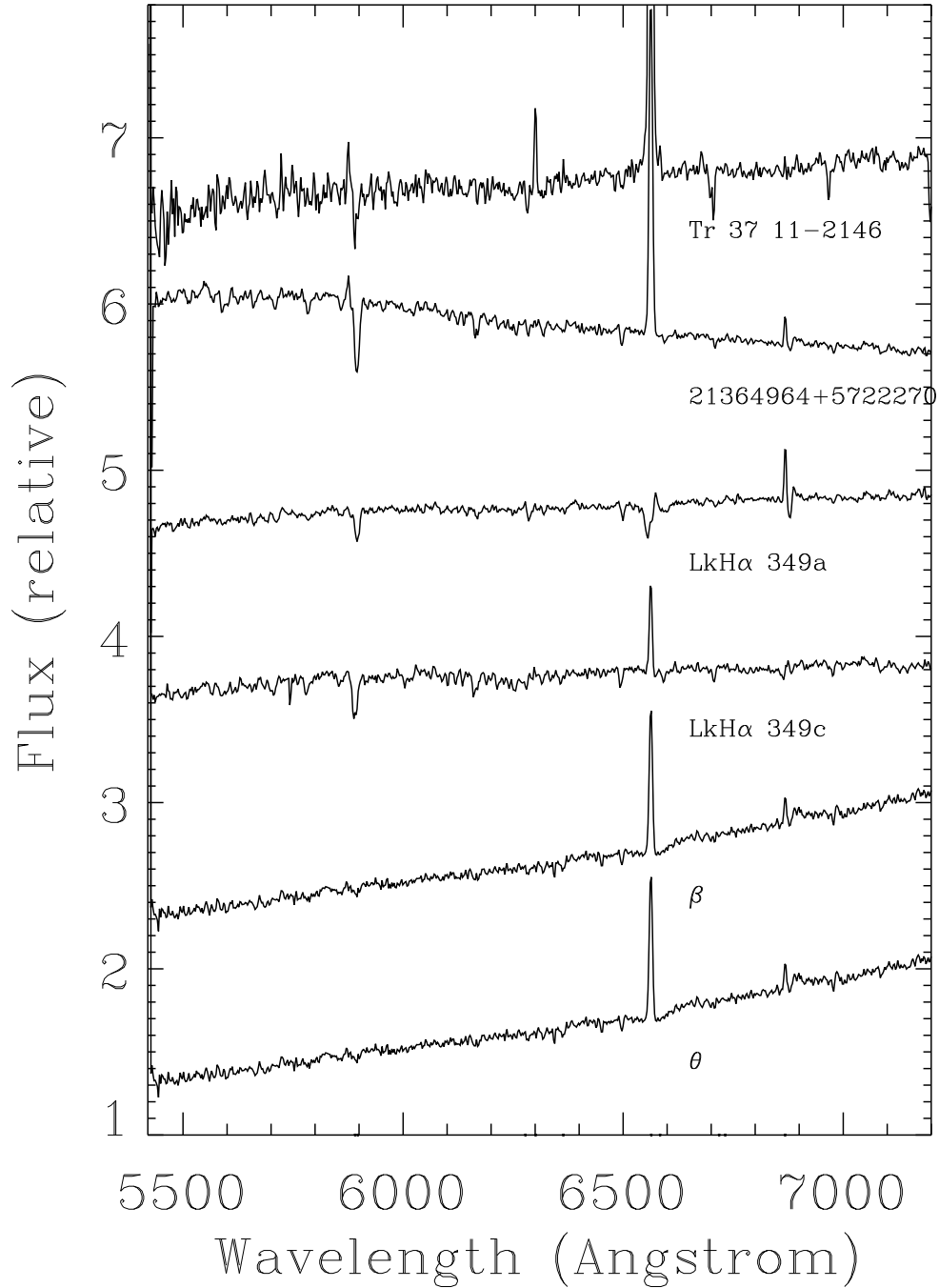


Fig. 11.— Optical spectra of Class II sources in IC1396A. Each spectrum was normalized by its median, scaled by 0.8, and shifted by unity from the previous for clarity. The bright H α lines are evident for all sources, except LkH α 349a, which has a P Cygni-like line profile as had been seen by Cohen & Kuhi (1979).

in the optical spectrum, and the predicted $V-J=-0.15$ whereas the observed $V-J=3$. These could be reconciled if the extinction $A_V > 5$ to this star; the best-fitting radiative transfer model has $A_V = 8$. The determination of the stellar mass from the infrared luminosity is of course very model-dependent; a spectral type in the A–F range are possible. There are other intermediate mass stars in Tr 37, including B stars in the IC 1396A region with surrounding nebulosity, so it is not implausible that IC1396A: θ is a young, intermediate mass embedded within a dense clump of material that is not its envelope. These properties plus the bright $H\alpha$ line make IC1396A: θ plausibly a Herbig AeBe star (Waters & Waelkens 1998).

The spectral energy distribution of IC 1396A: β is also relatively flat in the mid-infrared, but its $24 \mu\text{m}$ flux is not high, which led us to assign a Class II photometric type. The spectra presented in this paper confirm that β is a T Tauri star and not a Class I protostar. The best-fitting radiative transfer model has a large line of sight extinction, $A_V = 6.8$, explaining the lack of bright optical counterpart and infrared-dominated SED. The spectrum of β shows faint PAH features, similar to those seen around other young intermediate-mass stars (Sloan et al. 2005), though bright nebular emission in IC 1396A may contaminate the spectrum at the PAH wavelengths.

The spectral observations of Class II sources show that the mid-infrared-selected sample, identified in Paper I, is dominated by highly reddened, pre-main sequence stars of a wide range of masses from $0.4\text{--}5 M_\odot$ and luminosities from $1\text{--}40 L_\odot$.

5. Interaction between the Protostars and Globule

5.1. Physical conditions in the globule

The present configuration of the globule comprises an ionized layer on the side facing the O star (evident in $H\alpha$ emission), a dense bright rim (evident in PAH emission), and a high-opacity region (evident in extinction and in mm-wave molecular emission). The dense region comprises a round ‘head’ (centered on LkH α 349) with a hole in its center, and ‘trunk’ extending to the SW of the head.

Let us denote properties of the ionized layer with subscript i . From radio observations, its emission measure (Matthews 1979)

$$EM_i = n_i^2 L_i = 2000 \text{ cm}^{-6} \text{ pc}, \quad (6)$$

where $L_i \sim 0.07$ pc is the thickness of the ionized layer; hence we infer the density $n_i \sim 160 \text{ cm}^{-3}$ and, assuming temperature $T_i = 10^4$ K, pressure $p_i/k = 2 \times 10^6 \text{ cm}^{-3}$ K. The ionized layer is maintained by the O 6.5 star, with the rate of ionizing photons incident on the surface of the globule equal to the case B recombination rate for gas with density n_i .

Let us denote properties of the globule interior with subscript g . The radius of the head $R_g = 0.51$ pc. From CO and ^{13}CO measurements, the column density $N_g \sim 1.5 \times 10^{22} \text{ cm}^{-2}$, and the velocity dispersion $\delta v_g = 2.1 \text{ km s}^{-1}$ (Nakano et al. 1989), from which we infer the density $n_g \simeq 5000 \text{ cm}^{-3}$ and pressure $p_g = 3 \times 10^6 \text{ cm}^{-3}$ K. Thus at present, the bright rim of the globule is in pressure balance with the ionizing layer.

However, when the O star first generated its H II region and illuminated the globule, the pressure would have been much higher than that of the ambient gas. The initial conditions of the medium surrounding the O star are unknown, but they need not have been exceptional in order to lead to the present configuration. For example, Gritschneider et al. (2006) showed that an initially randomly turbulent medium evolves into a ‘pillar’ type morphology, like IC 1396A or the famous pillars of M 16, due to the pressure and ionization of the O star. The region that became IC 1396A would have had an initial density higher than average.

After the O star was born (~ 4 Myr ago), the pressure of the H II region drove a shock into the proto-globule. Using the density of the ionized layer and globule now, and eq. 12-15 of Spitzer, L. (1978), the shock speed would be $\sim 2 \text{ km s}^{-1}$. Such a shock would reach the center of the globule in 3×10^5 yr. Of course the density of the proto-globule was initially lower, and the globule was initially larger. These effects approximately cancel: the shock velocity $\propto n_0^{-1/2}$, while for a globule of constant mass the radius $\propto n_0^{-1/3}$, so the shock crossing time $\propto n_0^{1/6}$, a very weak dependence on the initial density. When the shock reached

the center of the globule, a strong over-density developed there. Numerical simulations, e.g. the landmark ones by Lefloch & Lazareff (1994), show both the central concentration and instabilities leading to smaller fragments within the globule. During the $\sim 10^6$ yr period of compression, much of the globule mass becomes ablated in a ‘cometary’ phase. IC 1396A is presently in this phase, with stars of a wide range of mass forming from the over-pressured globule material.

5.2. Outflows and Globule Destruction from the Inside

The central hole in the head of the IC 1396A globule may be only one of several outflow-related structures in the globule. In the following subsections we discuss evidence for current outflows in the globule and for the shaping of the globule by outflows.

5.2.1. Central cavity and LkH α 349

In optical images, a relatively transparent hole, through which background stars are visible, surrounds the young star centrally located in the head of the IC 1396A globule. Some wispy nebulosity is present, with the appearance of reflection nebulosity. In molecular line images, the hole appears relatively vacant of material. Nakano et al. (1989) showed using high-resolution CO data that the central hole is indeed nearly devoid of molecular gas. In the *Spitzer* images, the hole also appears to be devoid of material, and furthermore shows a bright rim, with a particularly well-define ‘wall’ on its W side. The hole size is $45'' \times 58''$ (EW \times NS). The central star, LkH α 349a, has a spectral type F9e and effective temperature 6165 K (Cohen & Kuhi 1979; Hernández et al. 2004). The extinction toward the star is nontrivial (despite the nearly empty appearance of the hole). The extinction is mostly local to IC 1396A, as opposed to intervening line-of-sight interstellar dust (for which one expects less than 1 mag extinction at the distance of IC 1396), so the extinction curve may have high $R_V \sim 5$ typical of stars behind molecular clouds (as opposed to the random ISM value of 3.1). Using the $R_V = 5.0$ (3.1) extinction curve, Hernández et al. (2004) find LkH α 349a to be a 5.4 (3.0) M_\odot star with luminosity 270 (45) L_\odot . The preferred, higher-luminosity solution is near the birth-line (age ~ 0.3 Myr) and consistent with the other indications of the star’s youth such as the H α line, which has a P Cygni profile indicating a wind with $v_w > 300$ km s $^{-1}$. The width and shape of the emission and absorption lines suggest a very high rotation rate $v \sin i \simeq 190$ km s $^{-1}$, near the breakup speed; this may be related to its apparently high-speed wind. We note that LkH α 349a will be a late B- to early A- type star on the main sequence and is likely a very young Herbig AeBe star (Herbig & Rao 1974),

many of which have similar properties (reflection nebulosity, self-absorbed H α winds) and are associated with star clusters with age of order 1 Myr (Habart et al. 2003).

The location of the LkH α 349 inside the hole, and its high luminosity and youth, lead one to suspect the star could have cleared the hole. This can readily be shown to be plausible. If the star produced, for a time t_w , a mechanical luminosity, L_w , leading to a bubble of radius R_w , then (Castor, McCray, & Weaver 1975)

$$R_w = 0.44 L_w^{\frac{1}{5}} n_{g4}^{-\frac{1}{5}} t_{w5}^{\frac{3}{5}} \text{ pc}, \quad (7)$$

where $t_{w5} = t_w/10^5$ yr, $n_{g4} = n_g/10^4 \text{ cm}^{-3}$, and L_w is in solar luminosities. If the stellar wind generated the presently-observed hole, $R_w = R_h = 0.09$ pc, then we can solve for the mechanical luminosity

$$L_w \sim 2 t_{w5}^{-3} \left(\frac{n_g}{5000 \text{ cm}^{-3}} \right) L_{\odot}, \quad (8)$$

and, for a wind speed v_w , the required mass-loss rate

$$\dot{M}_w = 1 \times 10^{-7} t_{w5}^3 \left(\frac{300 \text{ km s}^{-1}}{v_w} \right)^2 \left(\frac{n_g}{5000 \text{ cm}^{-3}} \right) M_{\odot} \text{ yr}^{-1}. \quad (9)$$

Since $v_w > 300 \text{ km s}^{-1}$, the mass-loss rate required for LkH α 349a to blow a bubble in the globule is plausible, by comparison to other young stars. Class I sources with luminosity $\sim 10^2 L_{\odot}$ have winds with $L_w \sim 0.1\text{--}1 L_{\odot}$ (Stahler & Palla 2004). Such a wind would only need to be active for $\sim 10^5$ yr to provide momentum to sweep the cavity clear. The SED models for LkH α 349a and c indicate ages of 0.4 and 1.2 Myr, respectively, allowing time for their wind phase to have passed. LkH α 349a is rotating exceptionally rapidly (Hessman et al. 1995), and has little or no disk, perhaps enabling a relatively spherical and powerful wind. The star appears close to the stellar birth-line but is clearly exposed, suggesting that while young, the star is likely to have completed its main ‘wind-bearing’ Class 0 and I phases and resides within the bubble that it blew.

The existence of a bubble blown LkH α 349a provides supporting, circumstantial evidence that it could have been triggered by radiative driven implosion. If LkH α 349a and its bubble had existed *before* the formation of the O 6.5 star, the bubble would not have survived to this day. The shock front driven by the pressure of the expanding H II region would have reached the center of the globule long ago, as discussed above. Such a large-scale shock would likely have significantly distorted the cavity sent it downwind of the young LkH α 349a.

5.2.2. Water maser near IC1396: γ

Figure 1 shows water maser emission toward source IC 1396A: γ . 22 GHz H₂O masers are associated with Class 0 protostars, and only rarely (4%) with Class I sources, in a survey of such sources (Furuya et al. 2001). The mid-infrared spectrum of IC1396A: γ has the characteristics of a Class I protostar with a rapidly-forming star accreting material from within a dense envelope. Is the H₂O maser from an outflow caught ‘in transition’ from Class 0 to I? Or is the maser spot from a clump of gas far from the protostar?

As noted by Valdetaro et al. (2008), the maser spot is significantly offset from the IC 1396A: γ by 5000 ± 200 AU. The maser peak coincides with a faint infrared source in the IRAC images. The coordinates of the IRAC source are $21^h36^m07.8^s$ $57^\circ26'42.8''$, within $1''$ of the VLA maser position; we will refer to this source for convenience as IC 1396A: γ_b . The fluxes of γ_b at 3.6, 4.5, 5.8, and 8 μm are < 0.2 , 0.6 ± 0.1 , 1.5 ± 0.2 , and 1.2 ± 0.3 mJy, respectively; with most of the uncertainty due to blending with the much brighter source γ . The corresponding magnitudes are $[3.6]>15.3$, $[4.5]=13.7$, $[5.8]=12.2$, $[8.0]=11.8$. No counterpart was evident in the near-infrared images. By chance, the orientation of one of the mid-infrared (IRS) spectrograph slits covered the faint source. The spectrum of γ_b cannot be cleanly separated from that of γ , but it is clear that the emission from the source is *not* line-dominated. If the infrared source were a Herbig-Haro type object, where the jet is impacting a dense clump, then we would expect strong emission lines of H₂. The IRS short-low spectrum (where the faint source can be separated from γ) covers 5.2-14 μm and would contain the pure rotational H₂ S(2) through S(7) lines if they were present. Furthermore, there is no corresponding spot at the H₂O maser position in the near-infrared rovibrational H₂v=1-0 S(1) image. Therefore, the IRAC source corresponding to the maser is not a shocked clump of gas. It is also unlikely to be a background galaxy, based on the lack of PAH features that would be prominent at 6.2 and 7.7 μm modulo some small redshift. The IRS spectrum of the faint source is dominated by continuum emission, and it looks roughly similar to that of the γ ; the difficulty of separating the sources makes it impossible to study the spectrum in detail from the available data.

Therefore, it appears that the H₂O maser is not directly associated with the luminous infrared source IC 1396A: γ , nor is it an interaction spot between the outflow and nearby molecular gas. The faint mid-infrared source IC 1396A: γ_b may itself be a protostar powering an outflow responsible for the H₂O maser. At 24 μm , a very bright source clearly corresponds in position to the luminous source γ . There is an extension from this source at 24 μm that corresponds to the faint source seen with IRAC, but it is severely blended: the offset is $7''$ while the beam size is $5''$. We scaled and subtracted the point spread function to estimate the 24 μm flux of the fainter source as ~ 10 mJy, corresponding to $[24]\sim 7.1$; a very conservative

limit is $[24] > 5.9$. Combining the mid-infrared colors of γ_b and comparing to Figure 3 of Paper I (i.e. comparing to the locations of Taurus and IC 1396A young stellar objects), the H₂O maser source γ_b appears to be a low-luminosity Class I protostar. This brings back the original question of why a Class I protostar has an associated maser. Perhaps this low-luminosity source is a Class I/0 transition object.

The remarkable result is that the brightest (only known) H₂O maser in the globule is close to the second-most-luminous ($L_{MIR} = 1.6L_{\odot}$) Class I protostar in the globule, but it is actually positionally coincident with a separate, low-luminosity ($0.02L_{\odot}$) infrared source. The separation of 5000 AU is somewhat wider than a binary pair; if γ has a mass (star plus envelope) of $\sim 1M_{\odot}$ then the orbital speed would be 0.5 km s^{-1} , comparable to the velocity dispersion of the globule. Class I sources have been found to have a wide distribution of separations, and this potential pair would be among the widest (cf. Connelley et al. 2008). There are other low-luminosity infrared sources in this field, so the total population of protostars may be much larger than the bright mid-infrared sources identified by eye in Paper I. Such low-luminosity objects have been found in other nearby star-forming regions that were surveyed by *Spitzer*, including those in dense cores in L1014 (Young et al. 2004), L1448 (Kauffmann et al. 2005), and L1521F (Bourke et al. 2006); they have been interpreted as sub-stellar protostars though the envelopes may contain more than $1M_{\odot}$. The prototype of the class, L1014-IRS, was searched for H₂O masers on 7 epochs with no detection (Shirley et al. 2007). The detection of an H₂O maser from IC 1396A γ_b is the first for a low-luminosity object of this class. Masers luminosities have been found to correlate roughly with the bolometric luminosity of their driving protostars (Furuya et al. 2001; Shirley et al. 2007), with $L_{H_2O} = 3 \times 10^{-9}L_{\odot}$ and over an order of magnitude of scatter. One could simply use this scaling to estimate or constrain the luminosity of the source, despite the large scatter and wide range of variability (a factor of 180). For IC 1396A: γ_b , we would obtain $L_{bol} \sim 0.1\text{--}1L_{\odot}$ depending which epochs are averaged together. Such a luminosity is not inconsistent with the observed mid-infrared luminosity, though it does suggest that the much of the luminosity emerges in the far-infrared.

5.2.3. Molecular Outflow from IC 1396A: γ

The Palomar 2.12 μm H₂1–0 S(1) continuum-subtracted image shows two knots of emission near IC 1396A: γ . Figure 12 shows that these knots are located diametrically opposite each other along a line that passes through γ , a configuration strongly suggestive of a jet, powered by γ , that is striking molecular knots forming dense Herbig-Haro objects (Reipurth and Bally 2007). The short length of the outflow (in particular compared to pc-

scale outflows) is likely due to its propagation into dense walls of the globule. That the outflow is seen in H_2 but not other tracers is also likely due to the dense material the jet interacts with.

Further evidence for a molecular outflow is found from observations this source using the Arizona Radio Astronomy Observatory Submillimeter Telescope in the CO(3–2) line (23'' beam, including both γ and γ_b). Figure 13 shows a prominent blue wing; a two-component fit of narrow line typical of the globule plus a second Gaussian with a full width at half maximum of 7.9 km s^{-1} and peak antenna temperature 3.7 K.

The presence of outflows from young stellar objects in IC 1396 is not unique to the globule studied in this paper. Reipurth et al. (2003) found HH objects and a 0.6-pc scale outflow in IC 1396N. They find that HH 777 emerges from the dense globule into the H II region. In the following section we discuss the potential influence of outflows on IC 1396A.

5.3. Compartments within the globule due to outflows

The internal structure of the globule around IC 1396: γ (Figure 12) is complicated, but it can be described as follows. There is a bright ‘wall’ located directly $\sim 10''$ upstream (i.e. toward the central O star of the H II region) of γ , with a curved shape that appears to merge with two east-west filaments that pass $\sim 30''$ north and south of γ ; the filaments continue downstream of γ for $\sim 180'$ before merging with other structures in the globule.

Using the equations above, assuming the upstream wall is a boundary between the wind and the turbulent pressure of the globule (or the ionized layer surrounding the globule, which has comparable pressure), the required mechanical luminosity of the wind $\sim 0.02L_{\odot}$ and the mass-loss rate $\sim 10^{-7}M_{\odot} \text{ yr}^{-1}$ (assuming an outflow speed $\sim 30 \text{ km s}^{-1}$ typical of such outflows) if the wind has been active for 10^5 yr . Such a luminosity is plausible, as γ is a class I/0 source with luminosity $\sim 30L_{\odot}$, for which outflow mechanical luminosities $\sim 0.1L_{\odot}$ are typical (Stahler & Palla 2004). The shape of the cavity around γ , if it is wind-blown, suggests a significantly lower density on its downstream side. If we naively use the wind bubble radius equation for the upstream and downstream directions separately, then with a size some 18 times longer in the downstream direction, the density would be lower by a factor of 10^6 , meaning the region downstream from γ was already essentially empty, with $n < 1 \text{ cm}^{-3}$, compared to the rest of the globule. Thus it seems unlikely that the structure around γ is an asymmetric, wind-blown bubble. Rather, its appearance and physical properties suggest a wind blowing into a high-pressure front of dense globule material upstream, and expanding relatively freely downstream into a region of much lower density.

Could this shape be a wind bubble blown by γ and other nearby protostars? We can use the same type of estimate as in the previous section to estimate the wind properties. The globule is very optically dark near γ indicating a high column density. The H₂O maser line is narrow, but we cannot use this as an estimate of the wind speed because masers are highly localized spots within the outflow. Instead, a lower limit to the molecular outflow speed is obtained from the range of velocities observed for the H₂O maser, which spanned 5 km s^{-1} over the observed epochs (Fig. 1). The actual outflow velocity is likely to be much higher depending on projection effects (as the masers are only individual spots in the outflow and can only under-represent the true range of velocities) and the bias that the H₂O emission

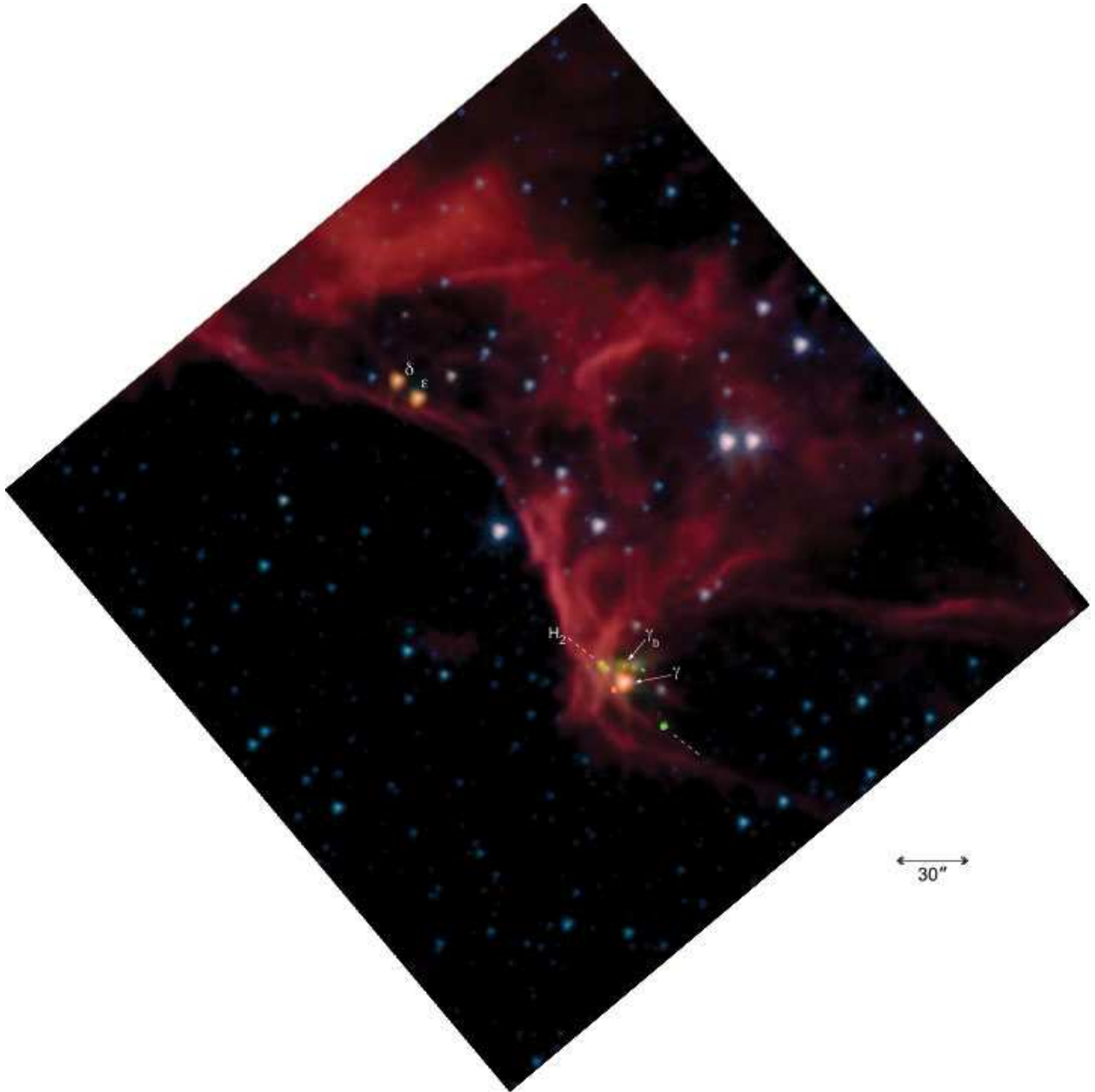


Fig. 12.— *Spitzer*/IRAC color image of the region around the protostar IC 1396A:γ. The 3.6 μm image is coded as blue, 4.5 μm as green, 5.8 μm as orange, and 8 μm as red. The Palomar/WIRC H₂ 2.12 μm image is coded as light green. Protostars IC 1396A:γ, δ and ε are labeled. Source γ_b is coincident with the 22 GHz H₂O maser. A small ‘×’ indicates an IRAC image artifact exactly 4.88'' (4 IRAC pixels) SE of γ. Dashed lines indicate the two shocked H₂ blobs on either side of source γ. The scale bar is 30''=0.11 pc=0.36 l.y.=22,000 AU long.

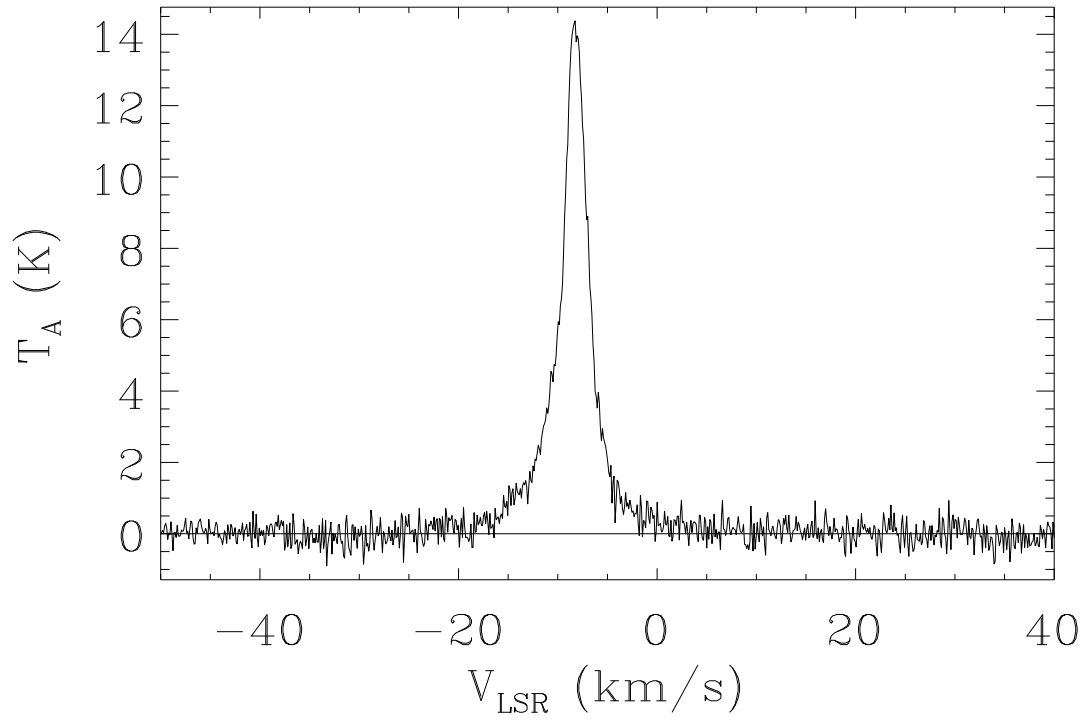


Fig. 13.— CO(3-2) spectrum of the protostar IC 1396A: γ .

traces only dense, warm molecular gas and not the likely ionized and much faster material closer to the star.

This empirical reasoning can be further extended to the rest of the globule. There are 5 prominent ‘voids’ within the globule and its main SE extension. All of the bright Class I sources for which we obtained IRS spectra are located within voids. The one containing γ was just discussed in the previous paragraph. The one containing δ and ϵ is similar in many ways to the one containing γ , in size, shape, and orientation. Since δ and ϵ are so close, it is possible that their winds combine to form this void. Three large voids are located within the globule head. These include the one containing Lk α that was discussed above, as well as one that contains protostar α . The third contains sources μ and ζ , with its E edge overlapping the globule edge; however, its NE boundary is clearly not the globule edge and has a curvature consistent with a roughly parabolic surface with μ at its focus and ζ near its edge.

Since the major voids all contain either mid-infrared-bright, Class I protostars, or the Herbig AeBe star in the globule hole, we suggest that the globule is being reshaped from the inside, with each protostar residing in a ‘compartment’ that it has blown via its outflow. Turning the argument around, we should see what influence each of the photometrically-defined Class I sources may have had on its environment. For this we consider the sources in the Class I region of the color-color diagram from Reach et al. (2004). In order of 8 μ m flux, these are α , γ , δ , ϵ , η , ζ , μ . All except η are accounted for in voids. Since η is located in a relatively busy portion of the globule, it would be difficult to separate any potential cavity from other overlapping structures. There are other, poorly-defined or smaller voids within the globule. One such void in the SW ‘trunk’ extension is located just W of $\delta+\epsilon$ and just N of γ ; this void is not as well defined and contains no mid-infrared source. Thus it appears that all (but one) of the Class I protostars are located within voids, and all (but one) of the voids contain Class I protostars or the Herbig AeBe star.

The evidence suggests that protostellar outflows are shaping the globule from the inside, while the pressure from the H II region maintains the bright rim in pressure equilibrium. The outflows may have a double significance. Not only are they destroying the globule’s structural integrity, leading to its further fragmentation and dissipation, but they may also drive and maintain turbulence, which would otherwise dissipate quickly in the dense gas, within the globule (Li & Nakamura 2006). This induced turbulence may be what prevents the entire globule from collapsing into stars, limiting the star formation efficiency.

5.4. Proplyd-like objects near IC 1396A

In addition to the protostars and wind signatures, the mid-infrared images contain features indicative of dense, starless cores. The term ‘proplyd’ was coined by O’de11 et al. (1993) to refer to protoplanetary disks made observable as silhouettes in HST images of the Orion H II region: a generic description would include a central star, an elliptical, dark patch, and a bright rim. Without a central star, we have a proplyd-like object that could be starless or harbor a protostar. There are numerous dark globules within IC 1396, ranging from the relatively large and bright ones like IC 1396A or IC 1396N (Reipurth et al. 2003) to smaller fragments dispersed throughout the H II region. We mention here some of the smallest ones, because the large, bright-rimmed globules contain multiple embedded infrared sources and do not meet the spirit of the definition as being produced by the circumstellar material of a single young star.

In the 10’ region around IC 1396A, there are several small clouds that have distinct *dark cores* surrounded by *bright rims* and often with cometary tails. These look similar to the proplyd-like objects in other H II regions. De Marco et al. (2006) studied those in 8 regions, finding that only one objects in M 17 contains a central star and may be a real proplyd (joining those originally found in Orion). Smith et al. (2005) explains the paucity of such objects outside Orion as being due to the short lifetime of the proplyd phenomenon. (Only Orion contains numerous stars < 0.5 Myr very close to the O stars.) Are the proplyd-like objects in IC 1396 and other H II regions small, individual-star-forming globules, or are they transient molecular cloud fragments en route to photoevaporation?

Figure 14 shows images of 5 proplyd-like objects in IC 1396, and Table 10 tabulates their properties. For objects A, B, C, and E, the position angle of the vector from the object to the central O star (O* PA) is nearly equal to the position angle of the vector from the tail to the head (Tail PA), indicating the tails are material ablated from the head, as is the case on larger scale for the IC 1396A globule. The central holes are marginally resolved with IRAC at $8 \mu\text{m}$, having diameters 5.0 to $15''$ compared to the PSF diameter of $2.4''$. For each object there is a distinct, dark ‘head’ that could be due either to a lack of material (i.e. an empty hole) or extinction. If we attribute the ‘heads’ as being dark due to extinction, then we require an optical depth at $8 \mu\text{m}$ $\tau_8 > 1$, which corresponds to $A_V > 10$ and $N_H \sim 1.8 \times 10^{22} \text{ cm}^{-2}$. The heads are not resolved in the MIPS images; the $24 \mu\text{m}$ image is consistent in morphology with a suitably smoothed and resampled $8 \mu\text{m}$ image (so the $24 \mu\text{m}$ morphology is consistent with either extinction or a central hole). The central volume density required in the heads are of order 10^6 cm^{-3} and masses of order $0.1 M_\odot$. The free-fall time is short (10^5 yr) in such high-density gas, but the cores can be supported if they have turbulent velocities around 0.2 km s^{-2} or a significant magnetic field. The properties of the heads are typical

of small dense cores in nearby star-forming regions (Myers, Linke, & Benson 1983). The analysis just presented is similar in nature to that of De Marco et al. (2006), who set the optical depth to H α emission to of order unity and concluded their proplyd-like objects are low-density and transient. In contrast, we find significant optical depth at 8 μm , requiring a significantly higher density. The near balance between likely turbulent and magnetic pressure versus gravitational force suggests the cores *may* indeed be forming stars. Their dynamical configuration, with a central density enhancement, bright rim, and ablated tail, suggest that the central core density could be higher than indicated at the angular resolution presented here, in which case that portion of the dense core will almost certainly collapse into a small star.

An alternative explanation for the proplyd-like objects is a standoff between a wind and the ionization front. In this case the deficit in brightness at the ‘head’ is due at least partially to a lack of material, instead of extinction. Using the same relations as in §5.2.1, the required wind mechanical luminosity $L_w = 0.002\text{--}0.09 t_w^{-3} L_\odot$. An outflow power of this order is typical for protostellar sources with luminosity or order 1 L_\odot . If the luminosity of such a source were emitted predominantly at 24 (70) μm , its flux would be of ~ 0.5 (1) Jy, which is clearly ruled out with the *Spitzer* data. The observed properties of the proplyd-like objects is therefore only consistent with being wind cavities if the embedded sources are significantly under-luminous (in photons) or high-powered (in wind). With the available information, we suggest the hypothesis previously mentioned, of an evaporating dense globule, is more likely.

While we described the objects as ‘proplyd-like’ based on analogy between their morphology and those of the silhouette protoplanetary disks in the HST image of Orion, another analogy is the evaporating gaseous globules (‘EGGs’) that are seen in many star-forming regions (Hester et al. 1996). The primary physical difference between EGG and proplyd is the lack of a bright central star, although even some EGGs are found to have low-luminosity stars or even outflows when observed at very high resolution. A point of distinction between these EGG-like objects is that they are not connected to a larger ‘pillar’ or globule that is being eroded by the ionization front. Instead, the objects we present here are isolated. They were most likely small regions of relatively high density that are currently being illuminated by the star, just like miniature versions of the IC 1396A globule. The proplyd-like objects discussed here are similar to the Thackeray’s globules in IC 2944, which appear to be starless (Reipurth et al. 1997). That these small globules lack indications of star formation in the *Spitzer* images shows that the mechanism of triggered star formation may not operate on the smallest globules, which may be evaporating so quickly (perhaps due to their larger surface area to mass ratio) that stars do not have time to form in their cores.

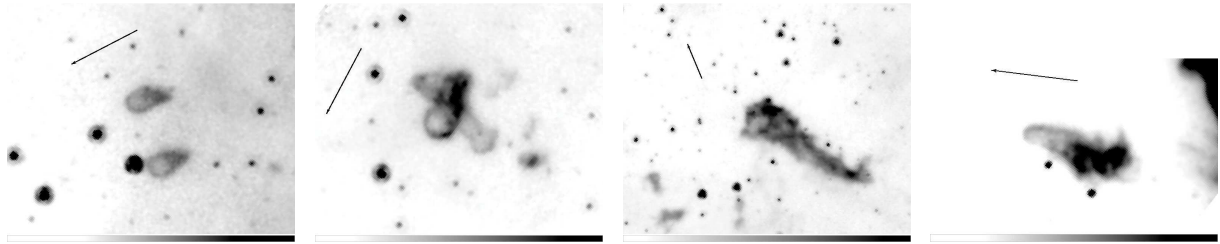


Fig. 14.— *Spitzer* 8 μm images of protoplanetary disk-like objects in IC 1396. Coordinates are given in Table 10; panel (a) contains objects A and B; panel (b) contains object C; panel (c) contains object D; and panel (d) contains object E. An arrow in each panel shows a 30'' long vector pointed toward the central O star HD 206267. All images are oriented with N up and E to the left.

6. Star formation in IC 1396A

6.1. Pre-Main Sequence ages for infrared-bright stars near IC 1396A

To determine the ages of the pre-main sequence stars near IC 1396A, we used the models from Siess et al. (2000) for a relatively high metallicity $Z = 0.04$, based on the assumption that the young Cep OB2 region should be more enriched than the cloud from which the Sun formed some 5 Gyr ago. Figure 15 shows the location on a color-magnitude diagram of the low-mass pre-main sequence stars within a $9'$ radius of IC 1396A from Sicilia-Aguilar et al. (2005) and from this paper. The photometry and extinction correction are not accurately known, so the large spread in H-R diagram and the precise locations of individual stars should not be over-interpreted. Taken at face value, LkH α c is very young (~ 0.5 Myr) and possibly coeval with the more-massive LkH α 349a (discussed in §5.2.1). The location of the source IC 1396A: θ can be only roughly estimated since it is not detected at 5500\AA ; for illustration we placed it at the location appropriate for $V=R+.5=17.5$. The mid-infrared sources tend to be younger than the optically-selected stars. Most of the stars are in the 1–5 Myr range, including the infrared-selected Class II sources for which Palomar and *Spitzer* spectra were obtained.

6.2. Generations of Star Formation in IC 1396A

Apart from LkH α 349, which formed near the center of the globule, the triggered star formation in smaller condensations may be expected to follow a sequence. For example, Sugitani, Tamura, & Ogura (1991) found an age gradient such that T Tauri stars lie closer to the triggering O star than *IRAS* sources, which tend to lie behind the bright rim. Matsuyanagi et al. (2006) showed this in detail for an individual bright rim. Does a similar sequence obtain among the young, mid-infrared sources in IC 1396A? There is a handful of Class I sources within IC 1396A—more than the typically 1 *IRAS* source for bright rims where the sequential trend was first noted (Sugitani, Tamura, & Ogura 1991). The youngest protostars in IC 1396A are likely those with the most ‘extreme’ infrared colors; these are ϵ , δ , γ , α , in order of increasing [8]-[24] (and [3.6]-[5.8]) color. The sources ϵ , δ , and γ are located just behind (0.02 pc) bright rims. On a larger scale, all of these protostars are located downstream of the center of the globule, and all but α are in the ‘trunk’ portion, known as SFO 36, which may have been swept back from the ‘head’ of the globule. The luminous Class I sources are further behind the bright rim than LkH α 349 and the hole it has carved from the center of the head of the globule. Thus it appears that the centroid location of the youngest protostars is significantly behind the main concentration of globule mass.

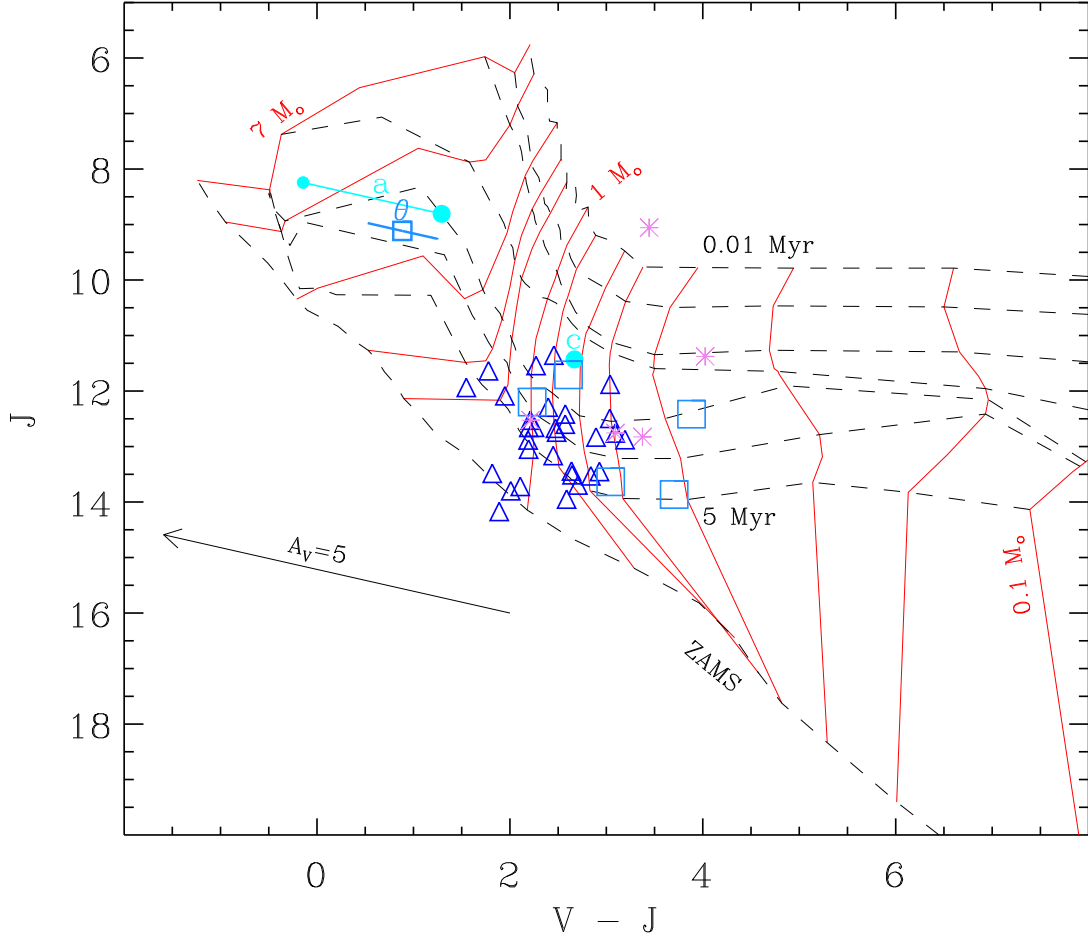


Fig. 15.— Hertzsprung-Russell diagram for IC 1396A, using theoretical models from (Siess et al. 2000) with $Z = 0.04$. Solid red lines are pre-main sequence Hayashi tracks for stars with masses (right to left) 0.1, 0.2, 0.3, 0.4, 0.5, 0.6, 0.8, 1, 1.3, 1.5, 1.9, 2.7, 5, and 7 M_{\odot} . The first 7 dashed black lines show isochrones for stars with ages (top to bottom) 0.01, 0.03, 0.1, 0.3, 1, 2, and 5 Myr; the lowest dashed line shows the zero-age main sequence (ZAMS). Two filled cyan circles linked by a cyan line labeled ‘a’ show the location of LkH α 349a for extinction curves with $R_V = 3.1$ and 5; the larger circle is the preferred, $R_V = 5$ result. A separate cyan filled circle labeled ‘c’ marks the location of LkH α 349c, on the 0.5 Myr isochrone and 0.6–0.8 M_{\odot} Hayashi track. Blue triangles mark the locations of low-mass pre-main sequence stars within the IC 1396A field (Sicilia-Aguilar et al. 2005). DodgerBlue-colored squares show the locations of the mid-infrared-selected (and optically detected) stars from Table 1; IC 1396A: θ is labeled and includes a line for a 1 mag range of extinctions. Violet asterisks mark the locations of stars just upstream of the bright rim of IC 1396A from Table 11.

Inspired by this observation, we searched for Class II young stellar objects just upstream from the bright rim. Indeed, there is such a set of infrared sources. We measured the mid-infrared fluxes of several of the 24 μm sources, and found the corresponding entries in 2MASS (J , H , K) and where possible in the tables by (Sicilia-Aguilar et al. 2005) (optical magnitudes, spectral type) or the USNO-A2 catalog.⁴ Table 11 lists the 4 sources with [8]j11. All of these sources are visibly exposed, despite being mid-infrared selected. For the 3 stars with spectra from Sicilia-Aguilar et al. (2005), emission lines make them classical T Tauri stars, with ages $> 10^6$ yr. A detailed study of such sources these sources is not possible without spectroscopy, because of variable extinction. One of the sources has essentially stellar color in the mid-infrared, but the optical counterpart is very faint (though it does have measured proper motion in the USNO catalog, indicating it is clearly not a background galaxy).

Figure 16 shows the distribution of sources photometrically identified as Class I and Class II using the *Spitzer*/IRAC and MIPS data from Paper I. The Class II sources are distributed throughout the region, while the Class I sources are clearly located within the globule. There may be a higher density of Class II sources toward the globule head and just upstream, though the number of sources is too small to determine if the over-density is significant.

Note that we do not see the same trend of locations of *near*-infrared sources relative to mid-infrared that Sugitani, Tamura, & Ogura (1991) found for some other bright rims. Whereas they found the sources with $J - K > 1.2$ are located preferentially upstream of the bright rim, we find instead that sources with $J - K > 1.2$, and also even redder stars with $J - K > 1.8$, tend to be located preferentially toward the globule. However, we do not believe this is a true association of large number of Class II YSOs with the densest part of the globule. Instead the distribution appears more consistent with a pattern of *extinction* of background sources, plus the Class I sources that are associated with the globule. To show this, we mapped the stars with more normal colors ($J - K < 1.2$), finding a fairly uniform distribution over nearly the entire region except toward the globule, which appears as a dramatic deficit of blue sources. In contrast, the distribution of red sources traces the globule accurately, and the number of red sources is exactly what is needed to ‘fill in’ the missing sources toward the globule. In §2.5 we described the extinction map generated from near-infrared source colors; this extinction map is very closely related to the distribution of CO and diffuse infrared emission. Similar extinction maps were obtained for IC 1396 globules by Froebrich et al. (2005). Therefore, it would be challenging to use a simple near

⁴From the USNOFS Image and Catalog Archive operated by the United States Naval Observatory, Flagstaff Station (<http://www.nofs.navy.mil/data/fchpix/>).

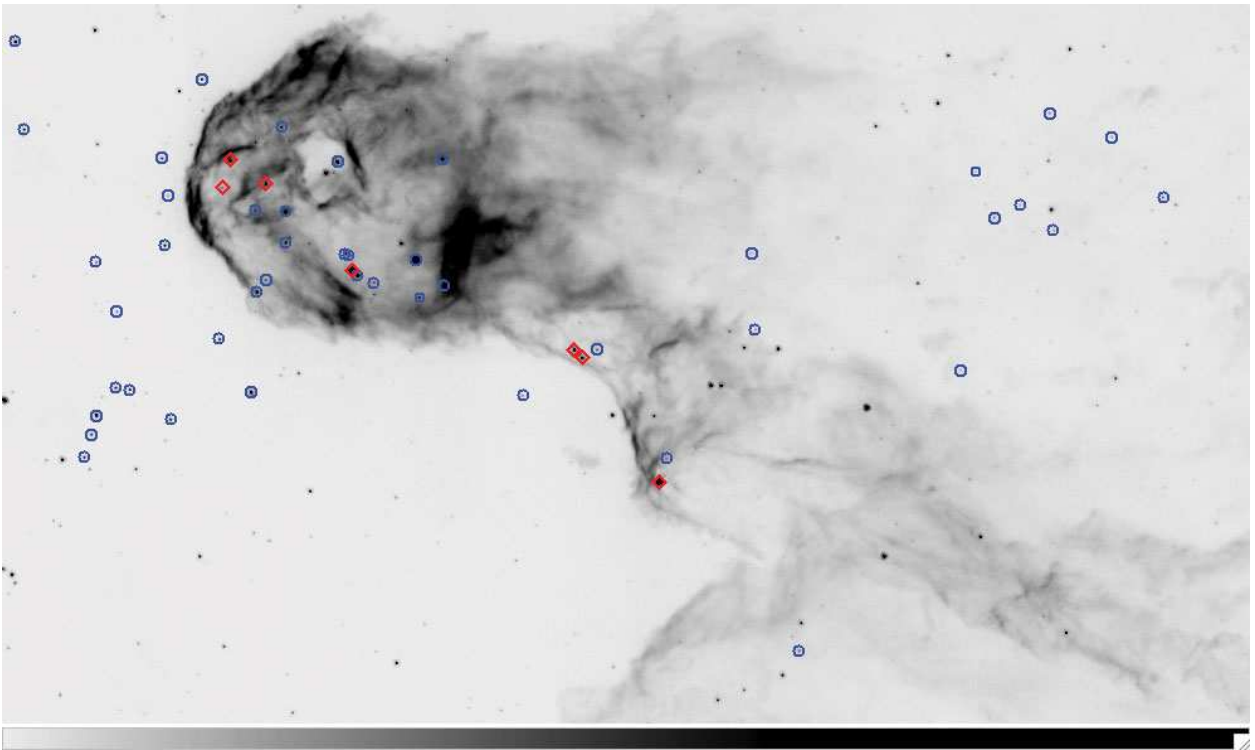


Fig. 16.— *Spitzer* 8 μm image of IC 1396A with sources photometrically identified as Class I enclosed in red diamonds, and those identified as Class II enclosed in blue circles.

infrared color criterion to select near-infrared sources as T Tauri candidates for IC 1396A.

With the available data, we can summarize that there are some mid-infrared-bright sources just upstream from the IC1396A bright rim, and most of these sources may be classical T Tauri stars. A small minority of the upstream stars may be highly embedded sources, but they are *much fainter* and less numerous than the Class I sources in the globule. There is a much wider distribution of Class II sources throughout the entire, large IC 1396 region. Thus we see some evidence for an age gradient versus density: the protostars are associated with the dense gas and the Class II objects are dispersed. Two possible mechanisms have been suggested for age gradients of this sort, and both of these mechanisms can work in concert. Stars that form earliest are gradually exposed as the pillar recedes due to progress of the ionization effect and ‘rocket’ acceleration in response to the ionized evaporative flow toward the exciting O star. While this scenario does appear to match the configuration for IC 1396A, in this scenario the young stars are expected to appear near the ‘tips’ of pillars (Hester & Desch 2005), whereas we observe the presently-forming stars further downstream. The other scenario is small-scale sequential star formation (Lefloch & Lazareff 1994; Sugitani, Tamura, & Ogura 1991), where the earliest stars to form in a globule actually contribute to the collapse and triggering of the next generation.

7. Conclusions

We studied a mid-infrared-selected sample of young stellar objects from *Spitzer* imaging (Paper I) using spectroscopic observations from radio to optical wavelengths. The photometric classifications in Paper I are confirmed by the spectroscopy. The Class I sources have deep silicate absorption features and the vast majority of their luminosity arises in the infrared. None of them show H₂O masers (characteristic of Class 0) or optical (Class II) counterparts. The only H₂O maser associated with our original sample turns out to be a separate object, IC 1396A:γb, with much lower luminosity $\sim 0.02L_{\odot}$ than the protostar we identified originally, IC 1396A: γ. The mid-infrared-selected Class I sources can be fitted with 0.1–2 M_{\odot} stars with ages $< 2 \times 10^5$ yr.

Compared to stars forming in the more quiescent Taurus molecular cloud, the physical conditions of the globule from which the stars are forming include a higher radiation field due to the O6 star exciting the H II region and nearby young B stars. There is also a higher pressure due to compression by the ionization front from the O6 star and winds from the many young and still-forming stars. The wind from the $\sim 5M_{\odot}$ star LkHα 349a has cleared a hole in the center of the dense globule, and outflows from the *Spitzer*-discovered Class I objects appear to have swept material into ‘compartments’ whose walls are over-pressured.

The spectroscopy results show that the Class I objects are brighter in the far-infrared than the theoretical models predict, suggesting they have a warmer envelope. Ice features in the Class I object envelopes differ somewhat from those seen around such objects in other star-forming regions. While the same set of features is present, their amplitude is lower, per unit silicate dust absorption, and the wavelengths are slightly shifted. Both of these effects suggest the Class I envelopes are warmer than in Class I sources in other star-forming regions, perhaps due to the warmer gas temperature in the star-forming material in the globule IC 1396A. The somewhat different physical conditions of the Class I envelopes in this globule will affect the chemistry at the time when planet formation is just beginning. Because the Sun is thought to have formed near an O star, and most nearby star-forming regions lack an O star, astronomical searches for the physical conditions of the early solar nebula would be best conducted in regions like IC 1396.

The stars photometrically classified as Class II are confirmed as such based on the presence of optical spectra with bright H α emission lines and mid-infrared spectra with silicate features in emission. Most of the disk spectra are similar to other commonly-seen T Tauri star spectra, dominated by amorphous silicates. But the star IC 1396A: θ has a particularly structured silicate feature with two ‘horns’ at 9.1 and 11.3 μm . The 11.3 μm horn can be explained by crystalline olivine. The origin of the 9.1 μm horn cannot be uniquely identified, with reasonably good fits provided by quartz (SiO₂), a phyllosilicate (montmorillonite), or $> 12 \mu\text{m}$ radius amorphous olivine grains. Similar spectra are evident in other wide samples of T Tauri stars. Such spectra show that the planet-building material around at least some stars is dominated by crystalline silicates and is significantly different from interstellar silicates.

The star formation history in IC 1396A cannot be described as a single “burst” of star formation: Class I and II sources in and near the globule span a range of ages and masses in a small region (2 pc across). It appears that the earliest star formation in IC 1396 occurred approximately 5 Myr ago, based on the ages of the Class II sources and the central O6 star. Some stars ahead of the present-day bright rim of IC 1396A have become exposed by the recession of the globule and by their own outflows. Recently, < 1 Myr ago, a powerful wind from the young AeBe star LkH α 349a blew a bubble through the center of the globule. The star formation in IC 1396A we observe now as Class I sources occurred within the last 0.2 Myr, based on the ages of the Class I sources.

The most recent star formation occurs preferentially behind the center of the globule, just inside bright rims. The specific trigger for the most recent star formation may have included not only pressurization of the globule by the O star exciting IC 1396, but also the pressure of outflows and jets from the earlier generation of stars and in particular those with

powerful winds like LkH α 349a. The young stars within IC 1396A appear to be reshaping the globule from the inside, clearing ‘compartments’ within the globule. Gradually, the globule is being fragmented due to the exponentially increasing number of stars (if indeed they are sequentially triggered). The mass contained in walls of the compartments will eventually become small enough, and their overlapping structure chaotic enough, that further star formation in the globule will end. The limiting factor in the star formation efficiency of this one globule will be the dynamic effect of energy input from the stars formed within it.

WTR gratefully acknowledges exceptionally valuable discussions with Bruce Elmegreen regarding the dynamics of the globule. Geoff Blake is thanked for assistance in obtaining the Keck/NIRSPEC *L*-band spectra.

This work is based in part on observations made with the *Spitzer Space Telescope*, which is operated by the Jet Propulsion Laboratory, California Institute of Technology under NASA contract 1407.

This work is based in part on observations obtained at the Hale Telescope, Palomar Observatory as part of a continuing collaboration between the California Institute of Technology, NASA/JPL, and Cornell University.

Some of the data presented herein were obtained at the W.M. Keck Observatory, which is operated as a scientific partnership among the California Institute of Technology, the University of California and the National Aeronautics and Space Administration. The Observatory was made possible by the generous financial support of the W.M. Keck Foundation.

This publication makes use of data products from the Two Micron All Sky Survey, which is a joint project of the University of Massachusetts and the Infrared Processing and Analysis Center/California Institute of Technology, funded by the National Aeronautics and Space Administration and the National Science Foundation.

REFERENCES

- Boogert, A. C. A. et al. 2008, ApJ, 678, 985
- Bourke, T. L., and 14 coauthors. 2006, ApJ, 549, L37
- Cambrésy, L., Beichman, C. A., Jarrett, T. H., Cutri, R. M. 2002, AJ, 123, 2559
- Castor, J., McCray, R., & Weaver, R. 1975, ApJ, 200, L107
- Cohen, M., & Kuhl, L. V. 1979, ApJS, 41, 743
- Connelley, M. S., Reipurth, B., & Tokunaga, A. 2008, astro-ph/0803.1172
- Decin, L., Morris, P. W., Appleton, P. N., Charmandaris, V., Armus, L., & Houck, J. R. 2004, ApJS, 154, 408
- De Marco, O., O’Dell, C. R., Gelfond, P., Rubin, R. H., Glover, S. C. O. 2006, AJ, 131, 2580
- Dorschner, J., Begemann, B., Henning, Th., Jäger, C., Mutschke, H.. A&A300, 503
- Draine, B. T., & Li, A. 2001, ApJ, 551, 807
- Fabian, D., Henning, Th., Jäger, C., Mutschke, H., Dorschner, J., & Werhan, O., A&A, 378, 228
- Froebrich, D., Scholz, A., Eislöffel, J., Murphy, G. C. 2005, A&A, 432, 575
- Furlan, E., Hartmann, L., Calvet, N., D’Alessio, P., Franco-Hernández, R., Forrest, W. J., Watson, D. M., Uchida, K. I., Sargent, B., Green, J. D., Keller, L. D., Herter, T. L. 2006, ApJS, 165, 568
- Furuya, R. S., Kitamura, Y., Wootten, H. A., Claussen, M. J., Kawabe, R. 2001, ApJ, 559, L143
- Gibb, E. L., Whittet, D. C. B., Schutte, W. A., Boogert, A. C. A., Chiar, J. E., Ehrenfreund, P., Gerakines, P. A., Keane, J. V., Tielens, A. G. G. M., van Dishoeck, E. F., & Kerkhof, O. 2000, ApJ, 536, 347
- Glotch, T. D., Rossman, G. R., Aharonson, O. 2007, Icarus, 192, 605
- Gritschneider, M., Naab, T., Heitsch, F., Burkert, A. 2006. in *Triggered Star Formation in a Turbulent ISM*, eds. B. Elmegreen and J. Palous, in press
- Habart, E., Testi, L., Natta, A., Vanzi, L. 2003, A&A, 400, 575

- Henning, Th., & Mutschke, H., A&A, 327, 743
- Hernández, J., Briceño, C., Calvet, N., Hartmann, L., Muzerrole, J. 2004, AJ, 127, 168
- Herbig, G. H., & Rao, N. K. 1974, ApJ, 174, 401
- Hessman, F. V., Beckwith, S. V. W., Bender, R., Eisloffel, J., Götz, W., & Guenther, E. 1995, A&A, 299, 464
- Hester, J. J., Desch, S. J., Healy, K. R., & Leshin, L. A. 2004, Science, 304, 1116
- Hester, J. J., Desch, S. J. 2005, in *Chondrites and the Protoplanetary Disk*, Eds. A. N. Krot, E. R. D. Scott, and B. Reipurth, (ASP: San Francisco), p. 107.
- Hester, J. J. et al. 1996, AJ, 111, 2349
- Higdon, S. J. U., Devost, D., Higdon, J. L., Brandl, B. R., Houck, J. R., Hall, P., Barry, D., Charmandaris, V., Smith, J. D. T., Sloan, G. C., Green, J. 2004, PASP, 116, 975
- Honda, M., Kataza, H., Okamoto, Y. K., Yamashita, T., Min, M., Miyata, T., Sako, S., Fujiyoshi, T., Sakon, I., Onaka, T. 2006, ApJ, 646, 1024
- Houck, J. R. et al. 2004, ApJS, 154, 18
- Hudgins, D. M., Sandford, S. A., Allamandola, L. J., & Tielens, A. G. G. M. 1993, ApJS, 86, 713
- Indebetouw, R., Whitney, B. A., Johnson, K. E., Wood, K. 2006, ApJ, 636, 362
- Kauffmann, J., Bertoldi, F., Evans, N. J., II, & the C2D Collaboration. 2005, Astron. Nach., 326, 878
- Keane, J. V., Tielens, A. G. G. M., Boogert, A. C. A., Schutte, W. A., & Whittet, D. C. B. 2001, A&A, 376, 254
- Kenyon, S. J., & Hartmann, L. 1995, ApJS, 101, 117
- Kessler-Silacci, J. E., et al. 2006, ApJ, 639, 275
- Kessler-Silacci, J. E., et al. 2007, ApJ, 659, 680
- Lefloch, B., Lazareff, B. 1994, A&A, 289, 559
- Nakamura, F. N., Li, Z.-Y. 2006, in *Triggered Star Formation in a Turbulent ISM*, eds. B. Elmegreen and J. Palous, in press

- Matthews, H. I. 1979, *A&A*, 75, 345
- McLean, I. S., et al. 1998, *Proc. SPIE*, 3354, 566
- Moriarty-Schieven, G. H., Xie, T., & Patel, N. A, *ApJL*, 463, L105
- Myers, P. C., Linke, R. A., Benson, P. J. 1983, *ApJ*, 264, 517
- Nakano, M., Tomita, Y., Ohtani, H., Ogura, K., & Sofue, Y. 1989, *PASJ*, 41, 1073
- O’Dell, C. R., & Wen, Z. 1004, *ApJ*, 436, 194
- Oke, J. B., & Gunn, J. E. 1982, *PASP*, 94, 586
- Osterbrock, D. E., Ferland, G. J. 2006, *Astrpphysics of gaseous nebulae and active galactic nuclei (2nd edition)* (University Science Books)
- Pontoppidan, K. M., et al. 2008, *ApJ*, 678, 1005
- Reach, W. T., Morris, P., Boulanger, F., & Okumura, K. 2003, *Icarus*, 164, 384
- Reach, W. T., et al. 2004, *ApJS*, 154, 385
- Reipurth, B., Corporon, P., Olberg, M., and Tenorio-Tagle, G. 1997, *A&A*, 327, 1185
- Reipurth, B., Armond, T., Raga, A., Bally, J. 2003, *ApJ*, 593, L47
- Reipurth, B., Bally, J. 2001, *Ann. Rev. Astron. Astrophys.*, 39, 403
- Rivkin, A. S., Howell, E. S., Vilas, F., & Lebofsky, L. A., in *Asteroids III*, eds. W. F. Bottke, Jr., A. Cellino, P. Paolicchi, & R. P. Binzel (Tucson: U. Arizona Press), p. 235
- Robitaille, T. P., Whitney, B. A., Indebetouw, R., Wood, K., & Denzmore, P. 2006, *ApJS*, 167, 256
- Schutte, W. A., & Khanna, R. K. 2003, *A&A*, 398, 1049
- Shirley, Y. L., Claussen, M. J., Bourke, . L., Young, C. H., & Blake, G. A. 2007, *ApJ*, 667, 478
- Sicilia-Aguilar, A. Hartmann, L. W., Hernández, J., Briceño, C., Calvet, N. 2005, *AJ*, 130, 188
- Sicilia-Aguilar, A. Hartmann, L. W., Watson, D., Bohac, C., Henning, T., Dullemond, C., Brandner, W. 2007, *AJ*, 132, 2135

- Siess L., Dufour E., Forestini M. 2000, *A&A*, 358, 593
- Skrutskie, M. F. et al. 2006, *AJ*, 131, 1163
- Stahler, S. W., & Palla, F. 2004, *The Formation of Stars*, Wiley, Weinheim.
- Sugitani, K., Tamura, M., Ogura, K. 1995, *ApJ*, 455, L39
- Sugitani, K., Fukui, Y., Ogura, K. 1991, *ApJS*, 77, 59
- Tachibana, S., Huss, G. R., Kita, N. T., Shimoda, G., & Morisha, Y. 2006l, *ApJ*, 639, L87
- Terebey, S., Shu, F. H., & Cassen, P. 1984, *ApJ*, 286, 529
- Matsuyanagi, I., Itoh, Y., Sugitani, K., Oasa, Y., Mukai, T., Tamura, M. 2006, *PASJ*, 58, 29
- O'dell, C. R., Wen, Z., Hu, X. 1993, *ApJ*, 410, 696
- Rhee, J. H., Song, I., & Zuckerman, B. 2008, *ApJ*, 675, 777
- Rho, J., Reach, W. T., Lefloch, B., Fazio, G. 2006, *ApJ*, 643, 965
- Sloan, G. C. et al. 2005, *ApJ*, 632, 956
- Smith, N., Bally, J., Shuping, R. Y., Morris, M., Kassis, M. 2005, *AJ*, 130, 1763
- Spitzer, L. *Physical Processes in the Interstellar Medium* (New York: Wiley)
- Valdettaro, R., Palla, F., Brand, J., & Cesaroni, R. 2005, *A&A*, 443, 535
- Valdettaro, R., Migenes, V., Trinidad, M. A., Brand, J., & Palla, F. 2008, *ApJ*, 675, 1352
- Vlemmings, W. H. T., & van Langevelde, H. J. 2005, *A&A*, 434, 1021
- Waters, L. B. F. M., Waelkens, C. 1998, *ARA&A*, 36, 233
- Whitney, B. A., Wood, K., Bjorkman, J. E., & Wolff, M. J. 2003, *ApJ*, 591, 1049
- Weikard, H, Wouterloot, J. G. A., Castets, A., Winnewisser, G., & Sugitani, K. 1996, *A&A*, 309, 581
- Weingartner, J. C., Draine, B. T. 2001, *ApJ*548, 296
- Werner, M. W. et al. 2004, *ApJS*, 154, 1
- Wilson, J. C. et al. 2003, *SPIE*, 4841, 451

Young, C. H. and 29 coauthors, 2004. ApJS, 154, 396

Table 1. Source list and observing log

Name ^a	RA DEC	Class ^b	IRS ^c	DBSP ^d	GBT ^e
IC1396A: α	21 ^h 36 ^m 46.6 ^s +57°29'38"	I	SL+LL+H	o	Y
IC1396A: β	21 ^h 36 ^m 55.2 ^s +57°30'30"	II	SL+LL	o	Y
IC1396A: γ	21 ^h 36 ^m 08.0 ^s +57°26'37"	I/0	SL+LL+H	o	Y
IC1396A: δ	21 ^h 36 ^m 19.3 ^s +57°28'38"	I/0	SL+LL	o	Y
IC1396A: ϵ	21 ^h 36 ^m 18.4 ^s +57°28'30"	I/0	SL+LL	o	Y
IC1396A: η	21 ^h 36 ^m 57.8 ^s +57°30'55"	I	SL+LL	o	Y
IC1396A: θ	21 ^h 36 ^m 39.2 ^s +57°29'53"	II	SL+LL+H	Y	Y
IC1396A: ι	21 ^h 36 ^m 36.8 ^s +57°31'32"	II	Y
IC1396A: κ	21 ^h 36 ^m 56.4 ^s +57°31'51"	II	Y
IC1396A: λ	21 ^h 36 ^m 54.8 ^s +57°30'00"	I	SL+LL	o	Y
IC1396A: μ	21 ^h 37 ^m 02.9 ^s +57°30'48"	I	Y
IC1396A: ν	21 ^h 36 ^m 57.9 ^s +57°29'11"	I/II	Y
IC1396A: ξ	21 ^h 35 ^m 57.9 ^s +57°29'11"	I/II	Y
IC1396A: ζ	21 ^h 37 ^m 02.3 ^s +57°31'15"	I	Y
LkH α 349c	21 ^h 36 ^m 49.5 ^s +57°31'22"	II	SL+LL+H	Y	...
LkH α 349a	21 ^h 36 ^m 50.7 ^s +57°31'10"	III	SL	Y	...
Tr37 11-2146	21 ^h 36 ^m 57.6 ^s +57°27'32"	II	SL+LL	Y	...
Tr37 11-2037	21 ^h 37 ^m 07.0 ^s +57°27'01"	II	SL+LL	Y	...
Tr37 72-1427	21 ^h 35 ^m 16.3 ^s +57°28'22"	II	SL+LL	Y	...
21361664+5728404	21 ^h 36 ^m 16.6 ^s +57°28'40"	II	SL	Y	...
21364964+5722270	21 ^h 36 ^m 49.7 ^s +57°22'27"	II	SL+LL	Y	...
Tr37 72-875	21 ^h 35 ^m 49.8 ^s +57°24'04"	II	SL+LL	Y	...
21364398+5729287	21 ^h 36 ^m 43.9 ^s +57°29'28"	II	SL+LL	Y	...
21362507+5727502	21 ^h 36 ^m 25.1 ^s +57°27'50"	II	SL+LL	Y	...

^aDesignations from IC1396A:x from Paper I, Simbad: [RRY2004] x; designations from (Sicilia-Aguilar et al. 2005), Simbad: [SHB2004] Trumpler 37 x-y; numeric designations from 2MASS All-Sky Point Source Catalog

^bClassification based on mid-infrared colors (Paper I).

^cObserved with the Spitzer/Infired Spectrograph; SL=5.2-14 μm , LL=14-35 μm , H=high-res (10-35 μm).

^dObserved with the Palomar 5-m/Double Spectrograph; Y=good spectrum, o=observed but not detected (no optical counterpart).

^eObserved with the NRAO Green Bank Telescope for 22 GHz H₂O masers.

Table 2. Brightness (magnitudes) of observed sources

Name	B	V	R	J	H	K _s	[3.6]	[4.5]	[5.8]	[8.0]	[24]
IC1396A:α	17.32	15.31	13.51	9.858	8.44	7.19	6.28	2.01
IC1396A:β	13.83	12.47	11.29	9.832	9.97	8.75	8.03	5.04
IC1396A:γ	19.76	...	13.95	10.56	9.22	7.84	6.80	2.24
IC1396A:δ	> 20	...	15.76	12.66	10.9	9.51	8.44	3.73
IC1396A:ε	> 20	...	16.95	12.57	10.9	9.16	8.55	4.27
IC1396A:ζ	16.48	13.62	10.84	9.86	9.02	8.84	4.48
IC1396A:η	17.08	15.41	14.05	12.40	11.36	10.6	9.15	4.93
IC1396A:λ	17.89	15.72	14.06	11.92	11.55	10.50	9.98	5.91
IC1396A:θ	17.0	11.73	10.21	9.50	8.414	7.85	7.21	6.53	4.07
LkHα349c	17.0	...	12.4	10.59	10.81	10.13	9.600	9.23	8.77	8.65	4.94
LkHα349a	15.2	...	11.4	11.71	8.95	8.62	8.440	8.44	8.25	8.14	...
Tr37 11-2146	17.1	16.92	15.6	12.07	11.52	10.82	9.932	9.69	9.13	8.34	4.89
Tr37 11-2037	16.3	16.03	15.1	12.58	11.72	11.29	10.87	10.59	10.2	9.51	4.49
Tr37 72-1427	...	18.08	...	14.03	13.07	12.67	12.08	11.89	11.4	10.8	6.81
21361664+5728404	17.02	15.06	13.98	12.29	11.57	10.8	10.0	7.22
21364964+5722270	16.8	...	14.9	12.84	12.07	11.79	11.38	11.51	10.9	10.3	5.73
Tr37 72-875	...	18.37	...	14.17	13.04	12.51	11.60	11.31	10.7	10.0	6.73
21364398+5729287	14.34	13.07	12.38	11.64	11.24	10.8	10.6	6.35
21362507+5727502	14.84	13.94	13.39	12.39	11.96	11.5	10.4	7.58

Table 3. Derived properties from optical spectra^a

name	$10^{14}I(\text{H}\alpha)$	$\text{H}\beta/\text{H}\alpha$	$A_V^{\beta/\alpha}$	A_V^{SED}	SpType	Age
IC1396A: α	1.12	0.134	3.6	10.1
IC1396A: β	0.86	0.12	4.1	14.0	F0 ^b	...
IC1396A: γ	1.05	0.19	2.3	(1.5)
IC1396A: δ	0.87	0.16	3.0	4.2
IC1396A: θ	1.28	0.071	6.0	3.8	A2 ^b	...
LkH α 349c	2.85	0.092	5.0	3.6	G9 ^b	...
Tr37 11-2146	4.71	0.10	3.4	1.5	K6.0	0.9
Tr37 11-2037	11.9	0.14	3.3	1.5	K4.5	2.5
Tr37 72-1427	4.8	0.15	3.1	1.5	M1.0	2.2
21361664+5728404	1.13	0.177	2.5	3.6
21364964+5722270	5.02	0.066	6.2	1.5	G5 ^b	...
Tr37 72-875	2.75	0.145	3.3	2.4	M0.5	8.4
21364398+5729287	2.41	0.071	6.0	7.1
21362507+5727502	3.26	0.17	2.7	1.7	M0.0	...

^aH α and H β fluxes were measured for each source. For the Class I objects, the spectra were extracted at the position of the infrared source and integrated over the appropriate wavelengths, but no optical counterparts were evident (so the lines are most likely nebular). Spectral types are from Sicilia-Aguilar et al. (2005)

^bapproximate spectral type based on luminosity

Table 4. 22 GHz Water masers in IC 1396A

Date	F_ν^{peak} (Jy)	F_{H_2O} (Jy km s ⁻¹)	L_{H_2O} (10 ⁻⁹ L _⊙)
2006 Aug 07	0.030	0.02	0.2
2006 Sep 28	0.042	0.06	0.7
2006 Nov 18	0.032	0.02	0.2
2007 Jan 24	0.29	0.28	3.7

Table 5. Mid-infrared spectral properties of protostars in IC 1396A^a

Source	[8]-[24]	[3.6]-[5.8]	α_{5-8}	$\Delta F_{10}/F$	$\Delta F_{15.2}/F$	$\Delta F_{6.0}/F$
Class I Sources						
IC1396A: α	4.27	2.66	-0.32	-0.64	-0.13	-0.08
IC1396A: γ	4.55	2.72	+0.19	-0.70	-0.10	-0.06
IC1396A: δ	4.70	3.15	+0.16	-0.79	-0.18	...
IC1396A: ϵ	4.27	3.41	-0.04	-1.00	-0.25	-0.17
IC1396A: η	4.22	1.75	+0.24	-0.31
IC1396A: λ	3.57	1.26	-0.12	-0.15
Class II Sources						
IC1396A: β	2.99	1.07	-0.26	...		
IC1396A: θ	2.45	1.19	-0.22	0.208		
LkH α 349a	1.62	0.82	-0.30	...		
LkH α 349c	...	0.18	-0.49	...		
Tr37 11-2146	3.44	0.79	-0.38	0.817		
Tr37 11-2037	5.01	0.63	-0.31	0.507		
Tr37 72-1427	4.08	0.58	-0.31	...		
21364964+5722270	4.61	0.38	-1.97	1.94		
Tr37 72-875	3.31	0.87	-0.03	...		
21364398+5729287	4.32	0.78	-0.95	...		
21362507+5727502	2.83	0.88	-0.15	0.625		

^a[a]-[b] is the color (magnitude difference) between bands a and b; α_{5-8} is the spectral slope $F_\nu \propto \nu^\alpha$ from 5 to 8 μm ; $\Delta F_\lambda/F$ is the amplitude emission (or absorption, if negative) feature, centered on wavelength λ (μm), relative to the local continuum.

Table 6. Ice Column Densities

Source	$N(\text{H}_2\text{O})$ 10^{18} cm^{-2}	$N(\text{CO}_2)$ % H_2O	$\tau_{9.7}$
IC 1396A α	1.6 (0.2)	14	1.12 (0.11)
IC 1396A γ	1.2 (0.2)	34	1.41 (0.14)
IC 1396A δ	4.3 (0.8)	23	1.96 (0.20)
IC 1396A ϵ	6.8 (1.7)	26	9.64 (1.00)

Table 7. Empirical model for Class I protostars in IC 1396A

	IC1396A: γ	α	δ	ϵ	Units
τ_{sil}	1.7	1.5	2.1	4.0	
A_V^2	24.5	21.6	30.2	57.6	
A_V^3	0.5	0.9	2.0	3.4	
R_{acc}	27	24	209	279	R_\odot
R_2	3.3	3.3	6.8	5.9	AU
R_3	9.5	1.8	1.6	1.7	10^3 AU
n_2	0.9	0.8	0.6	1.2	10^9 cm^{-3}
n_3	0.6	6.4	16.3	24.8	10^4 cm^{-3}
\dot{M}	2.3	2.0	4.1	7.3	$10^{-6} M_\odot \text{ yr}^{-1}$
L_1	2.7	2.7	0.6	0.8	L_\odot
L_{tot}	12.3	5.0	1.8	2.6	L_\odot

Table 8. Radiative transfer models for Class I protostars in IC 1396A

	IC1396A: γ	α	δ	ϵ	η	ζ	Units
Model ^a	3016360	3000224	3017673	3016207	3003269	3013344	
χ^2_ν	5.09	1.41	3.5	6.8	2.24	1.6	
\dot{M}	91.4	2.39	2.55	0.76	19.3	27.8	$10^{-6} M_\odot \text{ yr}^{-1}$
R_*	10.0	6.13	4.94	4.10	3.53	3.39	R_\odot
M_*	1.88	0.38	0.15	0.11	0.20	0.43	M_\odot
T_*	4321	3503	2839	2581	3062	3650	K
Age(*)	11.1	0.14	0.16	0.18	4.00	19.3	10^4 yr
L_{tot}	36.2	5.37	1.58	0.67	0.99	2.68	L_\odot
i	69.5	31.8	41.4	56.6	41.4	63.3	$^\circ$
A_V^{int}	65.2	62.9	64.3	73.6	26.5	30.4	mag (to central star)
A_V	7.4	1.4	8.0	7.4	4.4	4.4	mag (line of sight)

^aModel identification from Robitaille et al. (2006).

Table 9. Radiative transfer models for Class II protostars in IC 1396A

	21364964+5722270	IC1396A: β	LkH α 349c	LkH α 349a	IC1396A: θ	Tr37 11-2037	Units
Model ^a	3004629	3015197	3002727	3005288	3017958	3007956	
χ^2_ν	3.9	0.6	8.7	6.1	5.6	1.1	
M_{disk}	0.009	31.9	25.9	0.67	0.00007	0.26	$10^{-3} M_\odot$
\dot{M}_{disk}	0.007	68.2	70.9	0.01	0.002	1.53	$10^{-9} M_\odot \text{ yr}^{-1}$
R_*	1.77	2.34	4.41	3.63	2.67	2.24	R_\odot
M_*	1.50	0.80	0.70	2.28	4.99	0.80	M_\odot
T_*	5247	4123	3988	4829	16,450	4124	K
Age(*)	91.6	10.1	4.1	12.4	31.8	11.7	10^5 yr
L_{tot}	2.1	7.59	4.73	6.43	46.9	1.31	L_\odot
i	41.4	69.5	69.5	81.4	41.4	18.2	$^\circ$
A_V^{int}	0.002	0.016	0.85	0.003	0.001	0.011	mag (to central star)
A_V	2.8	6.8	1.80	1.60	8.0	1.40	mag (line of sight)

^aModel identification from Robitaille et al. (2006).

Table 10. Proplyd-like objects in IC 1396

Name	RA	Dec	O* Dist (pc)	O* PA (°)	Tail PA (°)	I_8 (MJy sr ⁻¹)	R_{hole} (AU)	L_{tail} (AU)
A	21 ^h 36 ^m 25.2 ^s	+57°39'48"	5.0	207	196	1.4	2000	10500
B	21 ^h 36 ^m 24.2 ^s	+57°39'22"	5.0	207	199	1.5	1900	9800
C	21 ^h 38 ^m 13.7 ^s	+57°40'30"	2.6	242	240	2.4	3300	14000
D	21 ^h 39 ^m 12.2 ^s	+57°24'07"	1.2	112	35	3.1	5600	74000
E	21 ^h 36 ^m 19.0 ^s	+57°26'59"	4.7	174	161	5.5	1900	25000

Table 11. Selected Infrared Sources Upstream from IC 1396A

2MASS	[24]	[8.0]	[5.8]	[4.5]	[3.6]	K _s	H	J	V
21370936+5729483	6.70	9.83	10.31	10.84	11.19	11.84	12.33	13.39	18.2
21371054+5731124	7.35	10.06	10.41	10.89	11.25	11.73	12.17	13.09	16.74
21370649+5732316	6.99	9.91	10.44	10.69	11.19	11.91	12.33	13.32	17.85
21371172+573329	6.95	10.78	10.73	10.88	11.06	10.90	11.12	11.94	17.4
21370802+5734094	7.66	7.970	...	8.01	7.74	7.86	8.37	9.62	14.5